Decoding Proteoforms with Single Acid Resolution Using a *Sub*-nanometer Diameter Pore

Tautvydas Lisauskas,[1#] *Archith Rayabharam,*[2#] *Punam Murkute,*[1] *Lisa Almonte,*[1] *Eveline Rigo,*[1] *Juan Oviedo Robles,*[1] *Zhuxin Dong,*[1] *Joshy Joseph,*[1] *Narayana Aluru,*[2] *and Gregory Timp*[1]*
[1]Electrical Engineering and Biological Science, University of Notre Dame, Notre Dame, IN 46556 USA
[2]Department of Mechanical Engineering, University of Texas, Austin, TX 78712-1229 USA
[#]contributed equally
*correspondence should be addressed to G.T. (email: gtimp@nd.edu)

Abstract. *When a denatured protein isoform* (*i.e., a proteoform*) *immersed in electrolyte is impelled by an electric field through a sub-nanometer-diameter pore* (*i.e., a sub-nanopore*) *spanning a thin membrane, the sequence of amino acid* (*AA*) *residues constituting the proteoform can be directly "read" one at a time by measuring fluctuations in the electrolytic current. Corroborating this assertion, an analysis of the pore current with molecular dynamic* (*MD*) *simulations reveals that the fluctuations are correlated to the sequence of AA volumes, the water in the pore and acid mobility. After alignment to account for variations in the acid mobility, the simulated pore current is nearly perfectly correlated to the pattern of empirical fluctuations. To prove out the prospects for decoding proteoforms this way, site-specific post-translational modifications* (*PTMs*) *and point mutations in amyloid-beta* ($A\beta_{1\text{-}42}$) *were analyzed with a sub-nanopore. The results show that single acids can be resolved in proteoforms with a dynamic range limited by the size of phenylalanine and glycine. With this sensitivity and single acid resolution, the sequence of a scrambled variant of* $A\beta_{1\text{-}42}$ *was discriminated with a p-value* $< 10^{-5}$.

Introduction.

Protein isoforms or proteoforms are proteins derived from closely related genes or post-translational modifications (PTMs) of them. Proteoforms may have related primary structures, but they can function very differently—even antagonistically. Yet apparently biology demands such diversity. It is estimated that there are about 100 isoforms per gene.[1-4] Since the structure dictates the function, based on these statistics, direct *de novo* sequencing of a protein seems essential to proteomics, but it is exacting work. Presently, proteomics relies mainly on Mass Spectrometry (MS)[5,6] to classify a protein and it typically requires more than a million copies to do it.[7-10] So, MS lacks the sensitivity and the dynamic range to detect less abundant peptides in a clinical specimen. Even if the peptide is correctly classified this way, the discovery of PTMs and their site assignments are still problematic; the sites are assigned statistically within a peptide.[11,12]

As an alternative to MS, it is now possible to directly "read", one at a time, the sequence of amino acids (AAs) constituting a denatured proteoform by impelling it through a *sub*-nanometer-diameter pore in a nanometer thick membrane, i.e. a *sub*-nanopore, immersed in electrolyte and measuring the pore current.[13-17] As the denatured proteoform, agglomerated with sodium dodecyl sulfate (SDS), moves processively through the *sub*-nanopore, the SDS is stripped from the proteoform and the ion flow around it fluctuates reproducibly in relation to the acids in the pore waist. If the pore current is sampled at a high enough rate (Ms/sec) in line with the acid velocity, and the electric field in the pore is confined to a *sub*-nanometer extent near the waist, then the fluctuations in the pore current inform on a single acid and the pattern of fluctuations reflects the AA sequence.

Several innovations have come together to put this alternative into practice. First, because the average volume of an AA residue is only about 0.15 nm^3, the amplitude of a fluctuation in the blockade scales like the molecular volume in the waist. So, a pore with *sub*-nanometer dimensions is indicated to recover a signal. Moreover, to recover the signal from a single acid, the electric field and therefore the current density must be tightly constrained to *sub*-nanometer dimensions consistent with the distance between AAs, which translates to a *sub*-nanopore in a nanometer-thick membrane. Second, when the pore current is sampled at a high rate, the signal is noisy due to the wide bandwidth. So, to reduce the noise, the wide bandwidth signal has to be averaged over clusters containing hundreds of blockades with similar fluctuation patterns.[18,19] The fluctuation patterns are identified using an affinity propagation (AP) algorithm without reference to any model for the peptide structure, unlike earlier work that compared the fluctuation patterns to a volume model of the sequence.[17] This distinction is important because it open a window into the identification of a protein in a mixture. Third, to call acids from the fluctuation patterns in the pore current, molecular dynamic (MD) simulations, which is

accomplished with atomic precision, are indispensable. An analysis of the pore current with MD reveals that the fluctuations are correlated to the sequence of AA volumes, their respective mobilities, and the water in the pore. Thus, MD can be used as basis for interpreting the fluctuation pattern with confidence, which is unprecedented. Finally, after accounting for differences in the acid mobility by using dynamical time warping (DTW) to align time sequence,[17,20-22] the empirical fluctuations in the pore current are nearly perfectly correlated to the MD simulations of the ion flow around a single acid translocating through the pore. The correlation between the aligned time sequence and the MD simulation of the current means that the acid sequence can be "read" with single acid resolution from the fluctuations with only a minimal amount of material—a few hundred molecules—required to identify a peptide. "Reading" a peptide with this resolution from so few copies holds out the prospect of changing proteomics.

To prove out the prospects for calling acids this way, an amyloid-beta peptide ($A\beta_{1\text{-}42}$) along with variants of it were analyzed with a *sub*-nanopore. $A\beta_{1–42}$ is the predominant species of amyloid-β (Aβ) affecting the pathology found in the brain of people with Alzheimer's disease (AD) and Down's syndrome. Aβ is supposed to accumulate in AD due to an imbalance in the production and clearance of the peptide resulting in the formation of amyloid plaques. Since there is no apparent change in the production of the Aβ peptide in AD, the propensity to form toxic species is likely driven by other factors besides just the primary structure of Aβ, such as the terminal acids, mutations and PTMs.[23-30] Importantly, aromatic residues like tryptophan (W) and phenylalanine (F) seem to drive amyloid formation *in silico*, but even non-aromatic acids such as cysteine (C) and methionine (M) reportedly produce amyloid-like structures.[28,29] Moreover, several PTMs have also been implicated in an increase in the aggregation rate, among them are phosphorylation of S8 and S26[24] and glycosylation.[30]

***Sub*-nanopore fabrication and characterization.**

A *sub*-nanopore sputtered through a thin amorphous silicon (*a-Si*) membrane was used to analyze the peptides. The native oxide that forms on amorphous silicon[31-34] motivated the choice of this membrane because: 1. it was apparently self-limiting and likely stabilized the pore topography; 2. it supposedly compensated for silicon surface states and thus, minimized the charge in the pore; 3. it was supposed to be negatively charged in water, which precluded bio-fouling; and 4. due to the silanol (*Si-OH*) on the surface, it was hydrophilic, which should ostensibly facilitate frictionless sliding translocation kinetics through the pore.[14] Although thin *a-Si* membranes were fabricated reproducibly with acceptable yield, they were fragile so the area of the membrane had to be minuscule to provide a margin for manufacturing. So, these membranes were only a few micrometers on-edge (Fig. 1a). Finally, the membrane thickness was especially important because it supposedly affected the field distribution in the pore and therefore the resolution of a "read" (supplemental note #1 and Fig. 1). Thin membranes that can support a large electric field were likewise important because a large electric force was required to lessen the prospect for backward steps in the motion of the acid through the pore to facilitate the interpretation of the blockade current. The thickness of the membrane was measured directly to be in the range from t = 3.5 to 6.0 nm (Fig. 1b) with transmission electron microscopy (TEM).

A *sub*-nanopore was sputtered through the *a-Si* membrane using a tightly focused, high energy (300 kV) electron beam formed in a scanning transmission electron microscope (STEM).[17] Immediately after sputtering, the pore was visualized *in situ* with TEM to reveal a 1.5 nm-diameter at the waist defined by the shot noise (Fig. 1c). However, when the same pore was re-acquired and the topography visualized with High-Angle Annular Dark Field (HAADF) using an aberration-corrected STEM after exposure to the ambient for 1–3 da, a smaller pore diameter was observed (Fig. 1d). According to the line profile, generally the pore topography had a steep

cone-angle > 5-15° that broadened to >16–30° near each orifice with an irregular waist > 0.40 nm in diameter. The pore topography was bi-conical, but since the STEM images revealed only the mass density under the probe beam, the angles indicated in the line profile represented twice the actual cone-angles.[17] According to this evidence then, the pore topography was likely affected, not only by electron-beam sputtering, but also by oxidation of silicon in the ambient. However, even though the STEM images were acquired at low voltage (80 kV) and/or with low beam current (16 pA), it was still possible that sputtering induced by the probe beam backfilled the pore.

Following earlier work,[16] finite element simulations (FES) that mimic the pore topography while accounted for the finite-size of the ion, the collapse of the electrolyte mobility and the negative surface charge were used to estimate the electric field distribution and electrolytic conductance through a *sub*-nanopore immersed in electrolyte. FESs revealed an electric field focussed to *sub*-nanometer dimensions near the waist (supplemental Fig. 1b). Depending on the cone-angle and membrane thickness, the electric field was supposedly focussed into a region about 0.70 nm in extent, which is about the size of a single stretched acid residue (0.5–0.55 nm).[14] The correspondence between the empirical conductance and the FESs lent credence to this idea (supplemental Fig. 1c). So, if only one (or two) acid(s) occupied the waist at a time, it was reasoned that the blockade current would mainly measure that residue. These assertions were corroborated by direct measurements of the force and the pore current as a single $A\beta_{1-42}$ molecule tethered to the tip of an atomic force microscope (AFM) cantilever was impelled through a *sub*-nanopore spanning a nominally 5 nm thick *a-Si* membrane (supplemental Fig. 2). That data revealed that the blockade was relieved (on average) about 1 nm before the electric force on the molecule terminated. This observation was interpreted as evidence that the current blockade occurs within about 1 nm of the waist since the electric field hardly extends

beyond that (supplemental Fig. 1). Finally, it has been shown empirically and corroborated with MD simulations that the ion mobility collapses as the diameter of the *sub*-nanopore shrinks[16] and so, it was reasoned that it would also affect the acid mobility and velocity in the same way.[35] Doubtless other AAs outside the waist still contributed at least marginally to the blockade current and the acid mobility in the pore, however.

Regardless of the length of the peptide chain, based on the median blockade duration, a peptide progresses through a *sub*-nanopore at an average rate of about one acid in 2 μsec. As an initial assessment of the read accuracy of a single blockade at this rate, current blockades sampled at 250 kS/sec and amplified over a bandwidth of 50-100 kHz associated with the translocation of three block copolymers: *block-p*$(R)_{10}$-*co*-$(G_3S)_3$-G, 23 AAs long (denoted by R-G-S); *block-p*$(K)_{10}$-*co*-$(G_3S)_3$-G, 23 AAs long (denoted by K-G-S); and *block-p*$(K)_{24}$-*co*-$(A_8P_8)_2$-A_8, 48 AAs long (denoted by K-A-P) were tested. These three block copolymers were used as positive controls because it was reasoned that the step in acid volume would show up as an abrupt change in the pore current (supplemental Fig. 3). Close scrutiny of single blockades of these controls revealed fluctuations consistent with the variations in the acid volume between *block-p*(R) and *co*-$(G_3S)_3$-G, and *block-p*(K) and *co*-$(G_3S)_3$-G and *co*-$(A_8P_8)_2$ in the copolymer, but despite the narrow bandwidth, the signal was still noisy, and the resolution blurred. Further improvement in signal averaging was indicated.

Besides the size, another feature that distinguishes *sub*-nanopores formed this way from proteinaceous nanopores (like MspA) is the resistance to chemical agents like sodium dodecyl sulfate (SDS) and β-mercaptoethanol (β–ME). SDS is an anionic detergent that works, in combination with heat (45–100°C) and reducing agents like BME, to denature proteins. The SDS molecule end-to-end is about 1.7 nm long and 0.25 nm wide. Ostensibly, the SDS binds regularly along the length of the protein backbone and imparts a nearly uniform negative charge

that swamps the intrinsic charges in the peptide, disrupting the native folded structure and producing a linear "rod-like" aggregate.[36] This is important because the acids constituting a peptide are not uniformly charged and so, the uniform charge on the protein-SDS aggregate is supposed to afford some control over the translocation kinetics through the electric force that develops when a voltage is applied across the membrane. The electric field then impels the aggregate progressively through the pore with a nearly uniform velocity, which facilitates "reading" the acid sequence without back-stepping. According to MD simulations, the SDS typically penetrates only about 1.2–1.3 nm into the pore during the translocation of the peptide across the membrane. However, due to the size of the aggregate, which is about 1.2–1.4 nm wide, the SDS is cleaved off by the steric constraints imposed by the pore topography leaving just a few acids exposed in the waist (Fig. 1f).[14] In contrast to the control afforded by a large electric field in a *sub*-nanopore, when a mutant MspA protein is used to "read" acid substitutions in a DNA-peptide conjugate, a motor enzyme—helicase Hel308—walking on the DNA is used to indirectly (through a linker) and imprecisely (due to helicase back-stepping) control the translocation kinetics of the peptide through the pore, which necessitates multiple reads of the same molecule to get it right.[37]

Detecting acid residues in measurements of the blockade current.

When a nearly pH-neutral (pH 6.6 ± 0.1) solution containing the denatured peptide was introduced on the *cis*-side of a *sub*-nanopore with a voltage of 0.4–0.7 V applied across the membrane, blockades (defined as: $\Delta I \equiv I - I_0$) were observed in the open pore current (Fig. 1e). Some, but not all, of these blockades were attributed to the translocation of a single peptide molecule across the membrane through the *sub*-nanopore (Fig. 1f). To interrogate each acid in the peptide, the blockade current was amplified over a wide bandwidth (1.8 MHz) and sampled at a rate (3.6 MS/s). The resulting signal was partially obscured by electrical noise (Fig. 1e) and

so, to identify the blockades the current traces were smoothed using a low-pass digital filter (Methods). To facilitate the analysis, the blockades were classified subsequently by the fractional change in the pore current relative to the open pore value ($\Delta I/I_0$) and the duration of the blockade (Δt). The aggregate data were then represented by a normalized heat map of the probability density function (PDF) reflecting the density and distribution of blockades (Fig. 1g). For example, the median blockade for the distribution delineated by the cross-hairs in Fig. 1g was at: $\langle \Delta I / I_0 \rangle = 0.16,\ \langle \Delta t \rangle = 100\ \mu\text{sec}$; the red contour captured 50% of the population.

Measurements of the fluctuations in the blockade current through a *sub*-nanopore were used to analyze eight different peptides (in addition to the three block co-polymers used for control): a 42-residue (human) amyloid-β ($A\beta_{1-42}$)-protein fragment and seven variants of it (supplemental Table 2). (The constituent acid residues comprising these peptides included nineteen of the twenty proteinogenic AAs; only proline was not included here, but it was included in the controls.) The blockade current distribution was important for accurate signal reconstruction. The fractional change in current has been linked to the ratio of the molecular volume to the pore volume according to: $\Delta I / I_0 = f \cdot \Delta V_{mol} / V_{pore} \cdot S$, where f measures the molecular shape and orientation, and S is a size factor that accounts for distortions in the electric field that occur when the molecule is comparable in size to the pore.[13,17,38] For the average acid volume constituting $A\beta_{1\text{-}42}$ (ΔV_{AA} = 0.13 nm^3) occluding the high electrical field full width at half-maximum (FWHM) stretch (0.7 nm long) in a bi-conical (10°) *sub*-nanopore with a mean diameter of 0.40 nm at the waist, it was estimated that $\Delta V_{1AA} / V_{pore} = 0.13 / 0.118 \approx 1 \propto \Delta I / I_0$, which overestimates the observed median fractional blockade. (Coincidently, on the other hand, if current crowding was ignored, and the molecular volume contained within the entire bi-conical pore (30°) spanning a 5 nm membrane is taken into account, then thirteen acids span the

membrane so that: $\Delta V_{13AA} / V_{pore} = 1.7/16.1 = 0.11 \propto \Delta I / I_0$.) Thus, based on these estimates, it was concluded that the empirical mean fractional blockade was consistent with a single molecule in the pore.

To inform on the sequence, ideally each acid should be sampled at the Nyquist rate, but if the acid velocity through the pore was variable then the sampling would not be uniform. The width of the blockade duration distribution relative to the median provides a hint about the molecular velocity variation. Based on the median duration of the translocation, the average velocity through the pore was about $\bar{v} = 2.3\times10^{-4} nm/ns (= 0.23\, mm/\sec)$. The force on an $A\beta_{1-42}$ molecule for a bias voltage of 0.7 V was measured directly to be (on average) about $\bar{F} = 25\, pN$ as it slid relatively frictionless through a *sub*-nanopore (supplemental Fig. 2).[14] The Einstein relation between the ionic mobility (μ) and the diffusion constant (D) predicts that: $D = k_B T\mu / q = k_B T\, \bar{v}^2 / \bar{F} = 5.7\times10^{-14} m^2/\sec$ and so, assuming a Gaussian profile, the ratio between the duration of a translocation and the FWHM of the distribution is given by: $2\sqrt{2\ln 2}(\sigma_t / \langle \Delta t \rangle) \cong 2.355\sqrt{2D / \langle \Delta t \rangle \bar{v}^2} = 0.72$. Thus, the width of the blockade duration distribution should be about 72% of the median, which corresponds closely to the width of the red contour shown (Fig. 1g) that represents 50% of the total population. In other words, Brownian diffusion accounts for the width of the distribution of the blockade duration.

The velocity fluctuations inherent in Brownian diffusion could confound a "read" if backward fluctuations in the acid motion through the pore exceed the distance between acids (i.e., if the molecule back-steps). According to the Nyquist criterion, the minimum bandwidth required to "read" each acid moving with a mean velocity of $\bar{v} = 2.3\times10^{-4} nm/ns$ is about 1.2 MS/sec. To avoid a back-step and a mistaken "read" then, the contributions to the root-mean-square thermal velocity fluctuations (up to 1.2 MHz), $\sqrt{v_{th}^2}$, must be smaller than the average

acid velocity or, in other words, $\bar{v}^2 > v_{th}^2 = (4k_B T\,\bar{v}/F)\cdot(\bar{v}/a) = \bar{v}^2 \cdot 4.114\,pN\cdot nm/(25\,pN\cdot 0.38\,nm) = 0.43\cdot\bar{v}^2$. Thus, a "read" error was tied to the ratio of the thermal energy to the work accomplished impelling an acid through the pore,[39] which is about $4k_B T/(Fa) < 0.4$ in these measurements. So, to avoid "read" errors due to back-stepping, a large electric force, *F*, was indicated, which translated to a short median duration $\langle \Delta t \rangle$ and a wide bandwidth amplifier for detection.

To improve the signal-to-noise ratio, a subset of the empirical data was selected for signal averaging by culling blockades with a duration too short to satisfy the Nyquist criterion or too long to preclude back-stepping. Likewise, blockades with a fractional blockade current too high ($\Delta I/I_0 > 0.3$) or too low ($\Delta I/I_0 < 0.10$) to be identified with a single molecule occluding the pore were also culled (Fig. 1g, red highlight). The mean of each of the blockades in the subset was zeroed and the result normalized by the standard deviation (σ) to form the Z-score. Then to recover reproducible fluctuations without any selection bias from irreproducible noise, two common signal-averaging techniques were employed: low-pass digital filtering; and signal averaging over clusters of blockades with similar fluctuation patterns[19,20] identified using an AP algorithm iteratively (Methods). Unlike the noise, fluctuations in the blockade current persisted even after signal averaging (Figs. 1h,i; red lines). Moreover, using the same *sub*-nanopores to acquire the data, differences in the fluctuation patterns between $A\beta_{1\text{-}42}$ and a scrambled variant of it (denoted as $SA\beta_{1\text{-}42}$), consisting of a different sequence of the same residues (supplemental Table 2), were conspicuous. On comparison, it was discovered that the empirical data were correlated with naïve volume models of the two peptides (Figs. 1h,i; blue lines) derived by translating the sequence of AA volumes ascribed to the primary structure obtained from crystallography data (supplemental Table 1),[40] assuming that the blockade current corresponded

to convolution over the sequence of volumes with a window k = 1-acid wide moving with a uniform velocity through the pore.[13,14] Strikingly, the amplitude of the fluctuations tracked closely the k = 1 volume models for $A\beta_{1\text{-}42}$ and the scrambled variant of it as indicated by the Pearson Correlation Coefficients (*PCCs*) *PCC* = 0.61 and 0.64, respectively. Yet, the empirical data for $SA\beta_{1\text{-}42}$ were poorly correlated to the volume model for $A\beta_{1\text{-}42}$ (*PCC* = – 0.050) and the $A\beta_{1\text{-}42}$ empirical consensus (*PCC* = 0.034). So, even though the number and constituency of AAs in the peptide did not change, the pattern of fluctuations did, and the pattern was correlated to volume models proving that the amplitudes were a measure of the acid sequence.

Parenthetically, to account for the current crowding near the waist of the pore, a convolution was performed over the AA volumes using a window k-acids wide that usually spanned between $1 \leq k \leq 2$ AAs, in correspondence with FESs of the electric field distribution. Then the width of the window was optimized to maximize the *PCC* between the model and the empirical data. However, convolutions with $1 \leq k \leq 2$ offered only a modest improvement in the *PCC* so, for clarity, the results presented here were compared to a k = 1 model exclusively, although it does not necessarily represent the optimum.

These results were especially relevant to the prospects for *de novo* sequencing of a protein for three reasons. First, the introduction of a bias in the data was avoided by using an AP algorithm to identify blockades with similar fluctuation patterns regardless of the pattern. Second, the differences evident between the consensuses representing $A\beta_{1\text{-}42}$ and $SA\beta_{1\text{-}42}$ indicate that the fluctuations patterns informed on the AA sequence of the respective peptides, which was consistent with earlier reports.[13,14,17] This means that the entire molecule could be sequenced at once this way, in principle, without resorting to enzymatic digestion, depending on an accurate interpretation of the fluctuations. Third, the correspondence between empirical consensus and the volume models proves that the fluctuations can be interpreted as high fidelity

"reads" with (nearly) single residue resolution. However, it is unlikely that all twenty AAs could be discriminated unambiguously based only on a volume model alone. (For example, leucine and isoleucine have practically identical volumes.) So, the correlation between the empirical consensuses and the corresponding volume models used for calling acids was still imperfect. Importantly, the underlying assumption in the comparison with the volume models was that the peptides moved through the pore with a uniform velocity, which seemed suspect because it discounted the possibility of variations in the acid mobility in the pore.

MD simulations of the translocation of A$\beta_{1\text{-}42}$.

To unravel the various components such as the acid volume, charge, mobility, and the effect of the neighboring acids and nearby water molecules to the amplitude and timing of the fluctuations, the pore current I, the acid mobility, μ, the radius of gyration (gyradius), R_g, the charge and hydration of each acid associated with the translocation of A$\beta_{1\text{-}42}$ and variants of it through a model of the *sub*-nanopore topography (Fig. 2a and supplemental VideoAB1-42e) were simulated with MD. These predictors were mutually related. For example, the fluctuation amplitude depends on the AA, which was affected by the acid volume relative to the size of the pore, the charge and the interactions between the molecule and the pore surface, coupled with the dynamics of the counter-ions, the neighboring acids, and water there.[41] In the simulation, the molecular force fields describing water, ions, and peptide fragments were combined with the CHARMM force-fields for the SiO_2 in a bi-conical *sub*-nanopore with a 0.4 nm diameter waist, which spanned a membrane 4 nm thick that separated an aqueous solution of *NaCl* into two compartments with a 5V bias between them (Methods). Accordingly, to economize on computing time, peptide fragments only one to four acids long occupied the pore waist at a time. This makes sense because, due to the size of the SDS-peptide aggregate, the SDS must be cleaved off in the pore waist exposing just a few acids. The translocation through the pore was

governed by several factors: the imposed (zero-acceleration) molecular velocity (5×10^{-6} *nm/ps*); the 5V difference across the membrane; and the non-bonding interactions of the peptide with the pore. The (5V) voltage drop across the membrane was important for three reasons: 1. it more closely mimicked the conditions of the experiment; 2. the electric force due to higher voltages distorted the acid volume in the pore, which destroyed the correlation to the empirical data; and 3. too few ions flowed around an acid residue in the pore waist for simulations performed at a lower voltage (0.5V), which compromised the statistical evaluation of the current. Although the course of these simulations were similar to the AFM experiments (supplemental Fig. 2) in which a single $A\beta_{1\text{-}42}$ molecule was impelled through a *sub*-nanopore, the duration of the empirical blockade (lasting ~ 30 sec at an applied voltage of 0.7 V), the measured force (~ 25 *pN*), and the molecular velocity were not captured precisely in these simulations.

Just like the empirical data, the properties of $A\beta_{1\text{-}42}$ calculated this way all fluctuated in correspondence with the acids in the pore waist (Figs. 2b-f, supplemental Table 1). The (negative of the) pore current was correlated to the AA volume (*PCC* = 0.77)[40] and the gyradius, R_g, (*PCC* = 0.72) that was calculated from the positions of van der Waals models for the atoms in the waist, the acid mobility (*PCC* = 0.60), and the number of waters near the acid (*PCC* = 0.71), but hardly related to the acid charge (*PCC* = 0.20). Likewise, the correlation between the simulated pore current and the acid volume extended to the variants. Coincidently, the magnitude of the pore current increased with the substitution of G for E22 (denoted by E22G), and decreased with the glycosylation of S26 (denoted by S26OGlcNAc), in correspondence with the changes in volume, mobility and waters in the pore. Specifically, corresponding to an increase (decrease) in the number of the waters in the pore waist, the mobility was diminished (enhanced) and the magnitude of the pore current swelled (shrunk). Generally, acid residues surrounded by a larger number of water molecules (such as A, S, D and G) tended to have lower mobility,

whereas acids surrounded by less water (K, R, F and I) showed higher mobility (assuming a linear fit, $R^2 = 0.54$). Also, larger acids (like W compared to G) squeezed out the water in the pore (assuming a linear fit to R_g, $R^2 = 0.92$). Incidentally, the number of waters in the pore estimated this way was not correlated (*PCC* = 0.026) to the WOPHS index, which was a measure of the acid hydropathy.[42] (According to WOPHS, the most hydrophobic acid residue, L, was rated 20 whereas the least hydrophobic, N, is rated 1.) The correlation between the mobility, the waters near the acid and the electrolytic pore current was rationalized by considering all the forces on the ions in the miniscule pore volume. As the peptide was impelled through the pore waist by the electric force, it dragged ions with it. Additional water in the neighborhood created drag that, in turn, slowed the residue. This coordination only happened because the ions, the water and the peptide (fragments) were constrained in the pore.

Importantly, the simulated pore current was also correlated to the empirical blockade current (*PCC* = 0.41). However, in this naïve analysis, the correspondence with the empirical data suffered because it was assumed that the velocity of the peptide through the pore was uniform; it did not account for the variations in the acid mobility. The acid mobility ranged from 12.4×10^{-3} to 15.3×10^{-3} $nm^2/V{\cdot}ns$, depending on the acid. So, if the speed of the acid through the pore was boosted or slackened, then the position in the time trace, τ_i, and duration of the ith fluctuation in the blockade current, $\Delta\tau_i = \tau_i - \tau_{i-1}$, would be affected by the mobility. To appreciate the disparities, $\Delta\tau_i$, was calculated for S26 ($\mu_{S26} = 12.5\times10^{-3}$ $nm^2/V{\cdot}ns$) and E22 ($\mu_{E22} = 15.3\times10^{-3}$ $nm^2/V{\cdot}ns$) subjected to the same electric field and then compared. Accordingly, whereas the average duration of a fluctuation per acid would be about $\Delta\tau = 2.4\mu s$, $\Delta\tau_{S26} = 2.7\ \mu s$ for S26 and $\Delta\tau_{E22} = 1.3\ \mu s$ for E22. Thus, the maximum deviation in the delay $\Delta\tau_i$, was about half the average.

Two conclusions follow from these simulations. First, the pore current was correlated to the size of the acid, the mobility and the waters surrounding the residues in the pore waist. Generally, the magnitude of the pore current decreased (increased) as the mobility increased (decreased), as the number of water molecules decreased (increased), and as the radius of gyration increased (decreased). The variation in acid mobility would undoubtedly affect the accuracy of a "read" since the acids would be crowded together or stretched apart in the blockade time trace. Second, although the volume difference may not easily be resolved, taken altogether, the other components affecting the pore current speculatively make it possible to discriminate between the acids. For example, although the volumes of isoleucine and leucine are practically identical ($V_{I,L}$ = 0.166 nm^3, R_{gI} =0.1833 nm, R_{gL} =0.1800 nm), the blockade current offered the prospect of resolving the two since I_L = 183.8 ± 42.1 pA, I_I = 137.9 ± 18.4 pA, so that ΔI_{L-I} = 46 pA. On the other hand, despite the volume difference, the largest amino acid residue, tryptophan (V_W = 0.228 nm^3, I_W = 131.3 ± 29.3 pA, μ_W = 13.5 ± 0.4 $nm^2/V{\cdot}\mu s$) was predicted to be difficult to discriminate from phenylalanine (V_F = 0.190 nm^3, I_F = 131.6 ± 22.9 pA, μ_F = 13.6 ± 0.4 $nm^2/V{\cdot}\mu s$) within the error based on the pore current or the acid mobility alone (supplemental Table 1). Likewise, it would be difficult to discriminate cysteine (I_C = 232.2 ± 3.9 pA, μ_C = 12.9 ± 0.1 $nm^2/V{\cdot}\mu s$) from alanine (I_A = 236.2 ± 11.2 pA, μ_A = 12.5 ± 0.1 $nm^2/V{\cdot}\mu s$) based only on the current or mobility. The similarity in the mobility of different acids extracted from these MD simulations may not be so representative, however. There was a threshold velocity below which the peptide fragment did not translocate through the pore.

Calling acids, point mutations and PTMs in proteoforms.

In principle, acids with a lower (higher) mobility require a longer (shorter) time to penetrate the waist, stretching (contracting) the position and duration of the ith fluctuation, $\Delta\tau_i$, in the blockade. To account for dilations or contractions, i.e. $\Delta\tau_1 ... \Delta\tau_i ... \Delta\tau_n$, that might result from

variations in the acid mobility, the fluctuations in the (normalized) time traces associated with Z-scored empirical consensuses were aligned to the corresponding MD simulations of the pore current (Methods). The DTW algorithm gauged the similarity between unsynchronized features in two time traces of the same length, n, and then performed a non-linear warping of the time axis to produce an optimal match between the positions of each feature through a search characterized by a symmetric step pattern through an $n \times n$ matrix containing the Euclidean distances between the points associated with a query and the reference.

DTW efficiently and accurately accomplished the alignment along the time axis, but it suffered limitations. For example, depending on the number of samples and the width of the warping window, DTW created so-called "singularities" when the amplitudes of the features in different time sequences varied.[22] These "singularities" developed when the algorithm tried to offset variability in the amplitude by warping the time-axis, which sometimes produced one-to-many mappings in which a single point in one time series was mapped to an entire sub-section of another. The endpoints were also important. Due to the boundary conditions that required the warping path to start and finish in diagonally opposite corners, DTW could be invariant to all warping, but still could not handle the difference at the start (or end) of the two time-series. This constraint meant that the algorithm was forced to match the pairs of beginning and end points, which adversely affected the statistical distance measure. So, to circumvent large variability in the endpoints, the algorithm used to identify a blockade was implemented with an extraction criterion (Methods). Finally, to avoid overfitting, each consensus was constrained to 500 samples and the warping window was restricted to a range of $\Delta\tau_i \leq 2.0$ AA positions or 24 samples out of 500.

As a first test of the DTW algorithm, an empirical query acquired from one *sub*-nanopore (LT111) was aligned to an empirical $A\beta_{1\text{-}42}$ reference sequence from another *sub*-nanopore

(PM13) to look for differences between the two (Fig. 3). This type of differential analysis was used as a test because it did not appeal to any model, but instead relied only on changes in the blockade current of the query measured relative to the reference to illuminate any differences in the acid sequence. It was compelling evidence of reproducibility that the normalized time sequence of the queries acquired from the same peptide, but with different *sub*-nanopores, were correlated to the reference (*PCC* = 0.32) to begin with (Fig. 3a, red and blue lines, respectively). Strikingly, however, alignment improved the correlation between the two (c.f. Fig. 3b) to near perfection (*PCC* = 0.96), although differences in the amplitudes at particular times still remained (c.f. Fig. 3f). Other *sub*-nanopores acquiring data from the same peptide performed similarly.

To call the acids from the features in the fluctuation patterns, the empirical consensuses were subsequently aligned to MD simulations of the pore current associated with the translocation of $A\beta_{1\text{-}42}$. To align the empirical consensuses to the MD model, the DTW algorithm compensated for local accelerations or decelerations by warping the time axis—shifting an acid-call in normalized time to the left (right) in the map to produce a shorter (longer) $\Delta\tau_i$ to compensate for a higher (lower) acid velocity in the pore waist. It was evident from the maps linking the queries to the reference model (Fig. 3c, red and blue lines) that both of the $A\beta_{1\text{-}42}$ empirical consensuses were indicative of a molecule progressing with a *nearly* uniform velocity through the pore (c.f. Fig. 3c, dashed black line), although deviations from a constant velocity were observed frequently. The largest deviations (< 24 samples) from a uniform velocity occurred in both pores near the N- and C-terminus of the peptide, likely due to threading peptide into the orifice

Once it was aligned (Figs. 3d,e), the warped empirical consensuses were observed to be highly correlated with the MD model for $A\beta_{1\text{-}42}$ (*PCC* = 0.95 for both). However, regardless of the high correlation, the acid with the smallest volume (V_G = 0.0599 nm^3), a practically neutral charge, and the largest number of waters in the waist, glycine (G9, G25, G29, G37 and G38),

was routinely overestimated in measurements (< 1.2 σ) relative to the model, but not always (G29 and G33). This deficiency likely represented a lower bound on the dynamic range of the measurement. In support of this assertion, serine (V_S = 0.0917 nm^3) was not usually overestimated. Curiously though, phenylalanine, leucine and isoleucine, with larger volumes ($V_{L,I}$ = 0.168 nm^3) and a lower number of neighboring waters in the waist compared to glycine, were often (but not always) underestimated in the measurement (F4, F19, F20, L17, I41). The deficiencies near the N- and C-termini might be attributed to irregularities in the molecular velocity and sampling associated with the peptide threading and vacating the pore, but tyrosine (Y10) with the largest volume (V_Y = 0.1912 nm^3) and a low number of waters in the waist was likewise underestimated relative to the prediction of the MD model. So, these deficiencies may instead represent an upper bound on the dynamic range of the measurement.

There were three salient aspects illuminated by this analysis. First, *sub*-nanopores with similar pore topographies produced correlated outcomes. The consensuses representing the same peptide acquired using different *sub*-nanopores (Fig. 3) with similar topographies produced correlated outcomes even without alignment, which indicated a (narrow) fabrication process margin for a *sub*-nanopore that makes large-scale manufacturing possible. Second, the nearly perfect correlation that developed between the MD model and the aligned empirical consensus means that the fluctuations translated to "reads" with single residue resolution,[17] which should facilitate calling the acids as it alleviates the analytical and computational burden associated with the identification of multiple monomers producing a fluctuation in a blockade.[13-15] Finally, despite the nearly perfect correlation, the dynamic range of a "read" measured relative to the MD-model seemed limited at high acid volume (F) when there were fewer waters in the pore, and at the low acid volume (G) when there was more water.

This type differential analysis with nearly single acid resolution was used to unambiguously discriminate between $A\beta_{1\text{-}42}$ and a scrambled variant, $SA\beta_{1\text{-}42}$, with the same acid constituency, but out of sequence. The empirical consensuses for $A\beta_{1\text{-}42}$ and $SA\beta_{1\text{-}42}$ consisting of 499 and 490 blockades were nearly perfectly aligned (*PCC* = 0.95 for both) to the corresponding MD models with a warping window $\Delta\tau_i$ = 2.0 AAs wide (Figs. 3b and 4a). However, just as it was in $A\beta_{1\text{-}42}$, glycine (G23, G27, G28 and G37 in $SA\beta_{1\text{-}42}$), was implicated in the measurements errors (< 1.6 σ) relative to the $SA\beta_{1\text{-}42}$ model (but not always G5 and G13 in $SA\beta_{1\text{-}42}$). Curiously, while isoleucine (I2) near the N-terminus was underestimated, the acids with larger volumes such as I18, I30, L10, and L36 were accurately appraised in $SA\beta_{1\text{-}42}$ in contradiction to the results obtained from $A\beta_{1\text{-}42}$. Since the same acids were just measured out of sequence, the discrepancies between $A\beta_{1\text{-}42}$ and $SA\beta_{1\text{-}42}$ suggest that neighboring acids may affect a "read".

To highlight the differences and, at the same time, check for consistency, the Z-scores of the aligned empirical data acquired from $SA\beta_{1\text{-}42}$ and $A\beta_{1\text{-}42}$ were subtracted. This type of differential analysis compounds the error, but tests the consistency of the measurement of each acid (relative to the models). Especially stringent conditions that tested the effect of neighboring acids occurred at sites 19, 37 and 42 where the two peptide sequences shared common acids (F19, G37 and A42). The nearly perfect correlation (*PCC* = 0.93) observed between the aligned empirical difference and the difference in the respective MD-models (Fig. 4b) testifies to the consistency of the measurement, although there were still discrepancies. The largest discrepancies occurred at site 4, implicating phenylalanine (< 0.4 σ), and sites 9, 23 and 38 that implicated glycine (< 1.5 σ). On the other hand, the signals attributed to F19, G37 and A42, which were common to both peptides, were accurately read—the same signals were measured with different neighboring acids. This evidence supports the idea that acids in the neighborhood

do not always appreciably affect a read. Regardless, signatures were evident in the blockade current fluctuations for both peptides that could be used to identify the sequence of the constituent AA residues. Despite the discrepancies, because the empirical differences so closely tracked the differences in the models, SA$\beta_{1\text{-}42}$ with the same constituent acids could be discriminated easily from A$\beta_{1\text{-}42}$ with a *p-value* < 10^{-5}.

Predicated on this type of differential analysis, to validate the acid assignments, other proteoforms of A$\beta_{1\text{-}42}$ were likewise assayed with a *sub*-nanopore. These proteoforms were selected to test the site specificity, the effect of neighboring acids, the sensitivity to the acid volume and hydropathy. To test site specificity, PTMs of A$\beta_{1–42}$ in which small, hydrophilic S8 and S26 acids were glycosylated with a large, hydrophilic O-linked β-*N*-acetylaglucosamine (denoted as S8OGlcNAc and S26OGlcNAc, respectively), were assayed and compared. Likewise, to test the sensitivity, S26 was phosphorylated (denoted by S26OPO_3) and then compared with S26OGlcNAc.

Both O-GlcNAcylation and phosphorylation can occur on the same serine residues, which suggests a complex biological relationship between the two PTMs. Like glycosylation (V_{GlcNAc} = 0.221 nm^3), phosphorylation also introduces a hydrophilic group in the side chain of serine, but it's miniscule in size by comparison (V_{PO4} = 0.056 nm^3). Correspondingly, MD simulations predicted an increase in the (negative of the) blockade ($I_{S8,26Gly}$ = 58.3 ± 28.2 *pA*) relative to serine in the A$\beta_{1\text{-}42}$ reference ($I_{S8,26}$ = 248.7 ± 45.7 *pA*), but a barely perceptible increase with phosphorylation (I_{S26PO4} = 196.7 ± 74.7 *pA*). So, phosphorylation of S26 (i.e. S26OPO_3) represented an especially stringent assessment of the sensitivity. The Arctic mutation of A$\beta_{1–42}$ in which a very small, hydrophobic G was substituted for a middling volume, hydrophilic E22 (denoted as E22G) was used to gauge the relative importance of volume and hydropathy. Following the same line of argument, it was conjectured that the difference in volumes between

E and the G substitution in E22G, (i.e., $\Delta V = V_E - V_G$ = 0.138 – 0.060 nm^3 = 0.078 nm^3, supplemental Table 1) would produce a reduction in the blockade current relative to $A\beta_{1-42}$. The MD simulations predicted a correspondingly large difference in the pore current ($\Delta I = I_E - I_G$ = 165.2 ± 19.3 *pA* – 386.9 ± 47.9 *pA* = –221.7 *pA*) and a discrepancy in the number of waters surrounding E (8.2) compared to G (10.2) (Fig. 2d and supplemental Table 1). However, E is charged and hydrophilic, whereas G is neutral and so, it was speculated that the mutation would test the effect of hydration as well as volume since the number of waters displaced from the pore by the acid was also supposed to affect the blockade current.[43] Another measure of the relative importance of volume and hydropathy was the mutant in which the small volume, neutral C was substituted for a very large volume, hydrophobic F at site 20 (denoted by F20C). MD predicted ($\Delta I = I_F - I_C$ = 131.5 ± 22.9 *pA* – 232.2 ± 3.9 *pA* = –100.7 *pA*) for this mutation. Finally, the Flemish mutation, F4W, provided the ultimate of the MD-model in which a neutral acid with the largest volume, W, was substituted for another large volume acid that was hydrophobic, F. MD simulations predicted practically no difference in the pore current ($\Delta I = I_W - I_F$ = 131.3 ± 29.3 *pA* – 131.6 ± 22.9 *pA* = 0.3 *pA*).

The empirical consensuses for these variants were aligned to the corresponding MD-models using DTW with a warping window $\Delta\tau_i \leq 2.0$ AA (24 samples) wide (Figs. 5a,c,e,g and supplemental Figs. 4a,c). Generally, the aligned empirical data was tightly correlated to the respective MD-models (*PCC* ≥ 0.90) with the usual exceptions. The pore current assigned to glycine (G9, G25, G29, G33, G37 and G38) was routinely, but not always, overestimated relative to the model, whereas the current attributed to isoleucine (I31, I32, I41), leucine (L17) and phenylalanine (F19, F20) were (sometimes) underestimated. To highlight the differences, the Z-scores of the aligned empirical data, acquired from each of the variants and $A\beta_{1-42}$, were

subtracted. Commensurate with the predictions, the difference in the Z-scores for S26OGlcNAc and S8OGlcNAc revealed prominent (> 2.1σ) peaks at S26 and S8 (Figs. 5b,d) that were attributed to glycosylation there. Although a prominent peak (1.7σ) was observed in the difference between the Z-scores associated with the aligned S26OPO3 and the $A\beta_{1\text{-}42}$ consensuses at S26 as well (Fig. 5h, red line), that identification was equivocal. Consistent with the simulations, a nadir in the Z-score (3.5σ) of the empirical consensus for the E22G mutation relative to the $A\beta_{1\text{-}42}$ reference was evident at site 22 (Fig. 5h, red line). Curiously, the measurement of the fluctuation amplitude attributed G22 in the mutant was assessed perfectly relative to the MD-model, as was G25. This was curious because measurements of all the other variants routinely overestimated G25 relative to the MD-model, but not in E22G. Based on this evidence, it was conjectured that acids three sites removed might influence a "read" and that even the smallest acid could provisionally be "read" accurately, depending on the sequence.

The accurate "reading" of the miniscule G prompted a chase to the bottom of the *sub*-nanopore sensitivity using the two mutants F20C and F4W (supplemental Fig. 4). A nadir was barely perceptible at site 20 in the difference in Z-scores for the aligned consensus acquired from the F20C mutant relative to the $A\beta_{1\text{-}42}$ reference (supplemental Fig. 4b), but the identification with the mutation was equivocal. Likewise, the difference between the F4W mutant and $A\beta_{1\text{-}42}$ consensuses at site 4 was not perceptible (supplemental Fig. 4d), but not expected according to MD, which predicted that $\Delta I = I_W - I_F = 0.3\ pA$.

Conclusion.

Taken altogether, these data, aligned to MD simulations, prove that measurements of fluctuations in the blockade current through a *sub*-nanopore when a proteoform is impelled through it are sensitive enough to "read" all the acids in the primary structure and identify point

mutations and PTMs in them precisely with single site specificity. The alignment exposed irregularities in the timing of the fluctuations, however, which were attributed to variations in the acid mobility in the pore in line with MD simulations. Although the *sub*-nanopores were not created with atomic precision, similar pore topographies produced correlated outcomes that indicated a (narrow) process margin for fabrication. Finally, the acid sequences were inferred from clusters formed from a few hundred blockades, which indicated that only a minimal amount of material was required to identify the peptide.

DATA AVAILABILITY

Summaries of the data generated and/or analyzed during the current study are included in the published article and the corresponding supplemental information file. Requests for these materials should be addressed to GT.

REFERENCES:

1. Abersold, R., Agar, J.N., Amster, I.J., Baker, M.S., Bertozzi, C.R., *et al.* How many human proteoforms are there? *Nat. Chem. Biol.* **14,** 206-214 (2018).
2. Gupta, N., Tanner, S., Jaitly, N., Adkins, J.N., Lipton, M., Edwards, R., Romine, M., Osterman, A., Bafna, V., Smith, R.D. & Pevzner. P.A. Whole proteome analysis of post-translational modifications: applications of mass-spectrometry for proteogenomic annotation. *Genome Res.* **17**, 1362–1377 (2007).
3. An, H.J., Froehlich, J.W. & Lebrilla, C.B. Determination of glycosylation sites and site-specific heterogeneity in glycoproteins. *Curr. Opin. Chem. Biol.,* **13**(4), 421–426 (2009).
4. Apweiler, R., Hermjakob, H. & Sharon, N. On the frequency of protein glycosylation as deduced from analysis of the SWISS-PROTdatabase. *Biochim. Biophys. Acta* **1473**(1), 4–8. (1999).

5. Nesvizhskii A.I. & Aebersold, R. Interpretation of shotgun proteomic data: the protein inference problem. *Mol. Cell. Proteomics*, **4**(10), 1419–1440 (2005).

6. Hughes, C., Ma, B. & Lajoie, G.A. *De novo* sequencing methods in proteomics. *Methods Mol. Biol.* **604**, 105-21 (2010).

7. Wells, G., Prest, H. &Russ IV, C.W. Why use Signal-To-Noise as a Measure of MS Performance When it is Often Meaningless? *Agilent Application Note* 5990-8341EN (2011).

8. Chait, B.T. Mass Spectrometry: Bottom-Up or Top-Down? *Science*, **314,** 65-66 (2006).

9. Valaskovic, G.A., Kelleher, N.L., McLafferty, F.W. Attomole Protein Characterization by Capillary Electrophoresis-Mass Spectrometry. *Science* **273**, 1199-1202 (1996).

10. Timp, W. & Timp, G. Beyond Mass Spectrometry, the Next Step in Proteomics. *Science Advances*, (2020) DOI: 10.1126/sciadv.aax8978

11. Savaryn, J.P., Catherman, A.D., Thomas, P.M., Abecassis, M.M. & Kelleher, N.L. The emergence of top-down proteomics in clinical research. *Genome Medicine* **5**, 53 (2013).

12. Kim, M-S., Zhong, J. & Pandey, A. Common errors in mass spectrometry-based analysis of post-translation modifications. *Proteomic*s **16**(5), 700-714 (2016).

13. Kennedy, E., Dong, Z., Tennant, C. & Timp, G. Reading the primary structure of a protein with 0.07 nm^3 resolution using a sub-nanometre-diameter pore. *Nat. Nanotech.* **11,** 968-976 (2016).

14. Dong, Z., Kennedy, E. & Timp, G. Discriminating Residue Substitutions in a Single Protein Molecule Using a Sub-nanopore. *ACS Nano* **11**(6), 5440-5452 (2017).

15. Kolmogorov, M., Kennedy, E., Dong, Z., Timp, G. & Pevzner, P. Single-molecule protein identification by subnanopore sensors. *PLoS Computational Biology*, **13**(5), e1005356 (2017).

16. Rigo, E., Dong, Z., Park, J.H., Kennedy, E., Hokmabadi, M., Almonte-Garcia, L., Ding, L., Aluru, N. & Timp, G. Measurements of the Size and Correlations between Ions using an Electrolytic Point Contact. *Nat. Commun.*, **10,** 2382 (2019).

17. Liu, X., Dong, Z & Timp, G. Calling the amino acid sequence of a protein/peptide from the nanospectrum produced by a sub-nanometer diameter pore. *Scientific Reports*, **12,** 17853 (2022).

18. Frey, B.J. & Dueck, D. Clustering by passing messages between data points, *Science*, **315**(5814), 972-976 (2007).

19. Hastie, T., Tibshirani, R. & Friedman, J. "The elements of statistical learning: data mining, inference, and prediction", Springer Series in Statistics (2009).

20. Giorgino, T. Computing and Visualizing Dynamic Time Warping Alignments in R: The dtw Package. *J. Stat. Soft.*, **31** (7), 1-24 (2009) doi:10.18637/jss.v031.i07.

21. Bagnall, A., Bostrom, A, Large, J. & Lines, J., The Great Time Series Classification Bake Off: a review and experimental evaluation of recent algorithmic advances. An Experimental Evaluation of Recently Proposed Algorithms. *Data Min. Knowl.. Disc.* **31,** 606-660 (2017). https://doi.org/10.1007/s10618-016-0483-9 Extended Version. http://arxiv.org/abs/1602.01711.

22. Keogh, E.J. & Pazzani, M.J. Derivative Dynamics Time Warping. **Proc. 2001 SIAM Int. Conf. Data Mining**, V. Kumar and R. Grossman eds.1-11 (2001). https://doi.org/10.1137/1.9781611972719.1

23. Kummer, M.P. & Heneka, M.T. Truncated and modified amyloid-beta species. *Alzheimer's Res. Ther.*, **6**, 28-37 (2014).

24. Russell, C.L., Koncarevic, S. & Ward, M.A. Post-translational Modifications in Alzheimer's Disease and the Potential for New Biomarkers. *J. Alzheimer's Disease,* **41**, 345-364 (2014).

25. Jana, A.K., Batkuwar, K.B., Klukarni, M.J. & Sengupta, N. Glycation induces conformational changes in the amyloid-β peptide and enhances its aggregation propensity: molecular insights. *Phys. Chem. Chem. Phys.*, **18**, 31446-58 (2016).

26. Halim, A., Brknmalm, G., Ruetschi, U., Westman-Brinkmalm, A., Portelius, E., Zetterberg, H., Blennow, K., Larson, G. & Nilsson, J. Site-specific characterization of threonine, serine, and tyrosine glycosylations of amyloid precursor protein/amyloid b-peptides in human cerebrospinal fluid, *Proc. Natl. Acad. Sci. U.S.A.* **108**(29), 11848-11853 (2011).

27. Schedin-Weiss, S., Winblad, B. & Tjernberg, L.O. The role of protein glycosylation in Alzheimer disease. *FEBS J.*, **281**, 46-62 (2014).

28. Gour, N., Kanth P., C., Koshti, B., Kshtriya, V., Shah, D., Patel, S., Agrawal-Rajput, R. & Pandey, M.K. Amyloid-like Structures Formed by Single Amino Acid Self-Assemblies of Cysteine and Methionine. *ACS Chem. Neurosci.*, **10,** 1230-1239 (2019)

29. Gazit, E. A possible role for p-stacking in the self-assembly of amyloid fibrils. *FASEB J.*, **16**(1), 77-83 (2002).

30. Smith, M.A., Richey, P.L., Taneda, S., Kutty, R.K.. Sayre, L.M.. Monnier, V.M. & Perry, G. Advanced Maillard reaction end products, free radicals, and protein oxidation in Alzheimer's disease. *Ann. N.Y. Acad. Sci.*, **738**, 447-454 (1994).

31. Zhang, M., Schmidt, T., Sangghaleh, F., Roxhed, N., Sychugov, I. & Linnros, J. Oxidation of nanopores in a silicon membrane: self-limiting formation of sub-10 nm circular openings. *Nanotechnology*, **25**(35), 355302 (2014).

32. Khalilov, U., Pourtois, G., van Duin, A.C.T. & Neyts, E.C. Self-Limiting Oxidation in Small-Diameter Si Nanowires. *Chem. Mater.* **24,** 2141-2147 (2012).

33. Fritzshe, H.; Tsai, C.C. Porosity and Oxidation of Amorphous Silicon films Prepared by Evaporation, Sputtering and Plasma-Deposition. *Solar Energy Materials* **1**, 471-479 (1979).

34. Ohsaki, H.; Miura, K.; Tatsumi, Y.; Ino, T. Structure of the Natural Oxide of Amorphous Silicon. Jap. *J. Appl. Phys.* **25**(12) 1773-1777 (1986).

35. Haridasan, N., Kannam, S.K., Mogurampelly, S. & Sathian, S.P. Translocation Mobilities of Proteins in Nanopores: A Coarse-Grained Molecular Dynamics Study. *Phys. Rev. E*, **87**, 062415 (2018).

36. Reynolds J.A. & Tanford, C. Binding of dodecyl sulfate to proteins at high binding ratios. possible implications for the state of proteins in biological membranes. *Proc. Natl. Acad. Sci. USA.*, **66,** 1002–1003 (1970).

37. Brinkerhoff, H., Kang, A.S.W., Liu, J., Aksimentiev, A. & Dekker C., Multiple rereads of single proteins at single-amino acid resolution using nanopores. *Science.* **374** (6574), 1509–1513 (2021). doi: 10.1126/science.abl4381

38. Qin, Z.P., Zhe, J.A. & Wang, G.X. Effects of particle's off-axis position, shape, orientation and entry position on resistance changes of micro-Coulter counting devices. *Meas. Sci. Technol.* **22**, 045804 (2011).

39. Lu, B., Albertorio, F., Hoogerheide, D.P. & Golovchenko, J.A. Origins and Consequences of Velocity Fluctuation during DNA Passage through a Nanopore. *Biophys. J.* **101**(1): 70-79 (2011). doi: 10.1016/j.bpj.2011.05.034

40. Perkins, S.J. Protein volumes and hydration effects. *Eur. J. Biochem.* **157,** 169–180 (1986).

41. Muthukumar, M. Communication: Charge, diffusion and mobility of proteins through nanopores. *J. Chem. Phys.* **141**, 081104 (2014).

42. Bonella, S., Raimondo, D., Milanetti, E., Tramontano, A. & Ciccotti, G. Mapping the Hydropathy of Amino Acids Based on Their Local Solvation Structure. *J. Phys. Chem. B.* **118,** 6604-6613 (2014).

43. Bhattacharya, S., Yoo, J. & Aksimentiev, A. Water Mediates Recognition of DNA Sequence via Ionic Current Blockade in a Biological Nanopore, *ACSNano,* **10,** 4644−465 (2016).

ACKNOWLEDGEMENTS: This work was mainly supported by a grant from the Open Philanthropy Project, and partially supported by the Keough-Hesburgh Professorship. Aberration-corrected STEM was accomplished at the Materials Research Laboratory Central Research Facilities at the University of Illinois in Urbana, IL with the assistance of J. Mabon and C.Q. Chen. We gratefully acknowledge discussions with Xiaowen Liu (Tulane University), Jun Li (Notre Dame) and Winston Timp (Johns Hopkins University).

AUTHOR CONTRIBUTIONS: G.T. conceived the experiments. T.L., P.M., L.A., Z.D., E.R., J.R. and G.T. performed the experiments and T.L., L.A., Z.D., E.R., J.R., J.J. and G.T. analyzed the data. A.R. and N.A. implemented the MD simulations in consultation with G.T. G.T. N.A. A.R., T.L., P.M., L.A., J.R., Z.D., E.R. and Z.D. all contributed to the manuscript and discussed the results.

COMPETING FINANCIAL INTERESTS: The authors declare no competing financial interests.

ADDITIONAL INFORMATION: Supplementary Information is available for this paper. The additional data is available in the on-line version. Correspondence and requests for materials should be addressed to G.T.

FIGURE CAPTIONS:

FIGURE 1. "Read" resolution and fidelity using a *sub*-nanopore through a thin *a-Si* membrane. (a) A transmission electron micrograph (TEM) is shown of a thin *a-Si* membrane spanning a 0.56 μm × 1.59 μm window through a 100 μm thick silicon handle wafer. **(b)** A TEM of a fold in a thin *a-Si* membrane after it was purposefully punctured to reveal a 5.3 nm thickness. The *a-Si* membrane was nominally 5 nm thick, but typically the thickness ranged from 3.5 to 6 nm. **(b, Inset)** A low magnification micrograph is shown of the fold in the membrane (b). **(c)** A TEM image taken *in situ* of a pore immediately after sputtering through a *a-Si* membrane. The cross-section of the pristine pore was estimated from the shot noise associated with electron transmission through the pore to be about 1.5 nm × 2.1 nm (dotted circle). **(d, top)** A HAADF-STEM image, acquired with an aberration-corrected STEM, is shown of the pore in (c) after exposure to the ambient. **(d, bottom)** The profile is shown taken along the dashed (horizontal) line in (d, top). The pore cross-section shrunk to about 0.4 nm × 0.7 nm likely due to the growth of a native oxide. The angles θ_1 and θ_2 reflect twice the cone angle of the bi-conical topography. **(e)** A current trace is shown that illustrates the blockade current associated with translocations of single molecules of $A\beta_{1\text{-}42}$ through a *sub*-nanopore measured with an applied voltage of 0.6 V. The pore current was amplified over a bandwidth of 1.8 MHz, filtered with a low pass 1 MHz filter and sampled at 3.6 MHz (gray line). Another version of the same data, smoothed with a low-pass 50 kHz eight-pole Bessel filter (black line), is juxtaposed on the 1 MHz data. The definition of the blockade current, ΔI, the blockade duration, Δt, and the open

pore current, I_0, are indicated. According to these definitions, higher current values correspond to larger blockade currents. **(f)** A visual molecular dynamics (VMD) snapshot is shown depicting the translocation of A$\beta_{1\text{-}42}$–SDS aggregate forced through a bi-conical *sub*-nanopore with a cone angle of 10° near the waist, spanning a 4.0 nm thick SiO_2 membrane. The diameter at the waist was 0.4 nm. The pore is ghosted in the figure; only the peptide, the SDS, the Na^+ (yellow/green) and Cl^- (cyan) ions and the water molecules are represented. Due to the steric hindrance, the SDS is stripped from the peptide near the pore waist. **(g)** A heat map is shown that illustrates the distribution of blockades relative to the open pore current ($\Delta I/I_0$) versus the blockade duration (Δt) associated with single denatured A$\beta_{1\text{-}42}$ molecules translocating through a *sub*-nanopore acquired at 0.6 V. The red contour captures 50% of the population and the red cross-hairs depicts the position of the median. The region highlighted in red indicates that portion of the distribution used to form the consensus. **(h)** A plot is shown of a blockade current consensus versus normalized duration measured when denatured A$\beta_{1\text{-}42}$ was electrically forced through a *sub*-nanopore (red line). The signals forming the consensus were acquired at 0.6 V amplified over a 1.8 MHz bandwidth, sampled at 3.6 MS/sec and digitally filtered to reveal the fluctuations. Juxtaposed with the empirical data is the corresponding volume model for the peptide (assuming $k = 1$, blue line). The blockade current was well correlated ($PCC = 0.61$) to the volume model. **(i)** Like (h), a plot is shown of a blockade consensus versus normalized duration acquired by electrically forcing a scrambled variant of A$\beta_{1\text{-}42}$, SA$\beta_{1\text{-}42}$, through the same *sub*-nanopore as in (h) (red line). Juxtaposed with the empirical data is the corresponding volume model (assuming $k = 1$, blue line). This empirical consensus was also well correlated ($PCC = 0.64$) with the volume model.

FIGURE 2. MD simulations of the translocation of A$\beta_{1\text{-}42}$ through a *sub*-nanopore in silica. **(a)** Visual molecular dynamics (VMD) snapshots are shown depicting three amino acid residues,

arginine (R), aspartic acid (D) and glycine (G) translocating through a *sub*-nanopore. The *sub*-nanopore that spanned a 4.0 nm thick membrane was defined by a bi-conical topography with a cone angle of θ_1 = 10° and a 0.4 nm diameter at the waist. The pore is ghosted in the figure; only the water molecules, the peptide fragments and the Na^+ (yellow/green) and Cl^- (blue) ions are represented. **(b)** The pore current derived from the MD simulations of the acids comprising the A$\beta_{1\text{-}42}$ (black) peptide impelled through the *sub*-nanopore are shown for each residue. **(c,d,e,f, black lines)** Like (b), the mobility, the number of waters in the neighborhood of the acid, the gyradius (R_g) and the charge extracted from MD simulations are shown, respectively.

FIGURE 3. Peptide sequence analysis of A$\beta_{1\text{-}42}$ using two different *sub*-nanopores. (a) Plots of two Z-scored empirical blockade current consensuses versus normalized duration are juxtaposed. These data were acquired at 0.6 V by forcing denatured A$\beta_{1\text{-}42}$ through two different *sub*-nanopores (denoted by PM13 and LT111) with similar topographies at transmembrane bias voltage 0.6 V and measuring the current. Although acquired from different pores, these two traces were correlated (*PCC* = 0.32). **(b)** The Z-scored empirical reference consensus associated with the translocation of A$\beta_{1\text{-}42}$ (blue line) through LT111 is shown versus normalized time. To improve the similarity with the reference, juxtaposed on the same plot is shown the dynamic time-warped (DTW) version of the Z-scored blockade consensus obtained from PM13 in (a) with a window $\Delta\tau_i$, = 2.0 AA wide for DTW. After DTW, the correlation improved to near perfection (*PCC* = 0.96). **(c)** The two empirical consensuses shown in (a) were warped to the reference MD model for A$\beta_{1\text{-}42}$ (red and blue lines). Mappings are shown to illustrate how DTW warps the time-line to improve the similarity. The diagonal (dashed black) line defines a uniform velocity and is used to highlight positional shifts or time delays, $\Delta\tau_i$, associated with acid mobility. **(d,e)** Using the mappings in (c), the Z-scored (left vertical axis) empirical consensuses acquired with LT111 and PM13 shown in (a) were aligned to the MD model for A$\beta_{1\text{-}42}$. The putative acid

positions are shown on the horizontal axis. The aligned empirical data is nearly perfectly correlated to the MD-model (*PCC* = 0.95), but there are "read" discrepancies associated with the smallest and largest acids. **(f)** For reference, the difference between the Z-scores of the two empirical consensus shown in (b), which were aligned to each other, indicating irreproducible noise between different pores. **(g)** The difference between the Z-scores of the empirical consensuses shown in (d,e) each aligned to the $A\beta_{1-42}$ MD model reference is shown versus the putative acid positions (red line). Juxtaposed on the same plot is the difference in Z-scores between the $A\beta_{1-42}$ MD models for each (blue line).

FIGURE 4. Sequence analysis of beta-amyloid ($A\beta_{1-42}$) and scrambled beta-amyloid ($SA\beta_{1-42}$) with single acid resolution using a *sub*-nanopore. (a) The aligned empirical consensuses for $SA\beta_{1-42}$ is shown versus the putative AA positions (red lines). The corresponding MD model is juxtaposed on the same plot (blue line). The consensus is well correlated to the model with *PCC* ≥ 0.95. **(b)** The differences in the Z-scores between the aligned consensus for $A\beta_{1-42}$ shown in Fig. 3e and the aligned consensus for the $SA\beta_{1-42}$ variant in (a) are shown versus the putative AA positions (red line). Juxtaposed on the same plot is the difference in the Z-scores between the respective MD models for $A\beta_{1-42}$ and the $SA\beta_{1-42}$ (blue line). The difference between the empirical consensuses were well correlated to the difference in the corresponding models (*PCC* > 0.93). Based on the close correspondence, the two variants could be discriminated with a *p-value* < 10^{-5}.

FIGURE 5. Proteoform sequence analysis with near single acid resolution using a *sub*-nanopore. (a,c,e,g) Empirical consensuses associated with blockades due to S26GlyNAc, S8GlyNAc, E22G and S26OPO3 are shown after alignment to the corresponding MD models versus the putative AA positions (red lines). Juxtaposed with the empirical consensuses are the corresponding MD models for each variant (blue lines). The dotted blue line indicates the site of

the mutation or PTM. The aligned consensuses were all well correlated to the respective MD models with *PCC* ≥ 0.90. **(b,d,f,h)**The differences in the Z-scores between the aligned consensus for $A\beta_{1\text{-}42}$ and the respective aligned consensuses for the variants in (a,c,e,g) (red lines) are shown versus the putative AA positions. (The $A\beta_{1-42}$ reference data used for comparison—see Fig. 3e—which was acquired with the same *sub*-nanopore, was nearly perfectly aligned with the respective MD model *PCC* = 0.95 as well.) Juxtaposed on the same plots are the differences in the Z-scores between the respective MD models for $A\beta_{1\text{-}42}$ and the corresponding variants (blue lines). The difference between the empirical consensuses were correlated to the difference in the corresponding models (0.26 < *PCC* < 0.82). The peaks prominent in (b,d) were attributed to the glycosylation S26 and S8. The nadir evident in (f) was attributed to the E22G substitution.

FIGURES
FIGURE 1

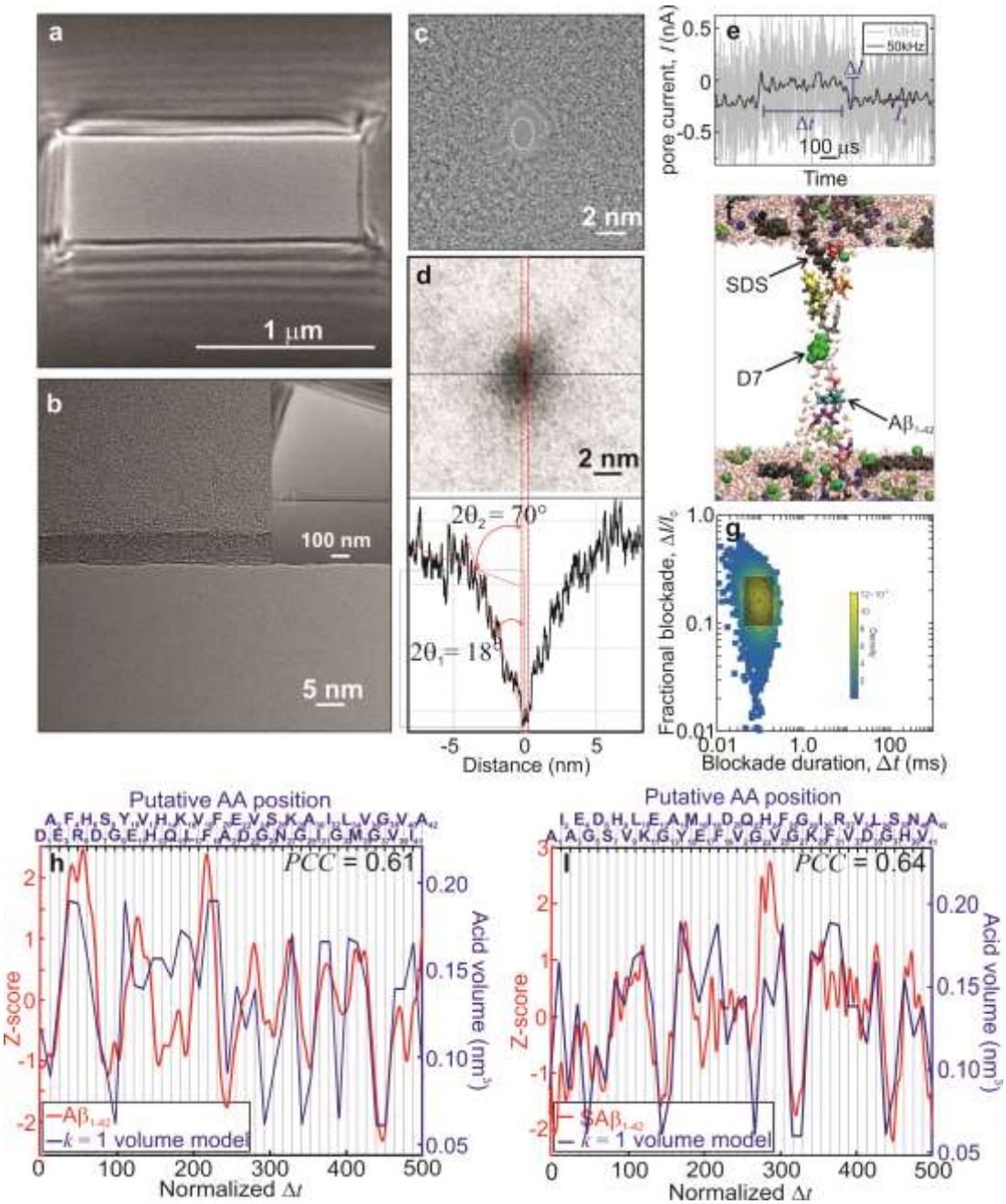

FIGURE 2

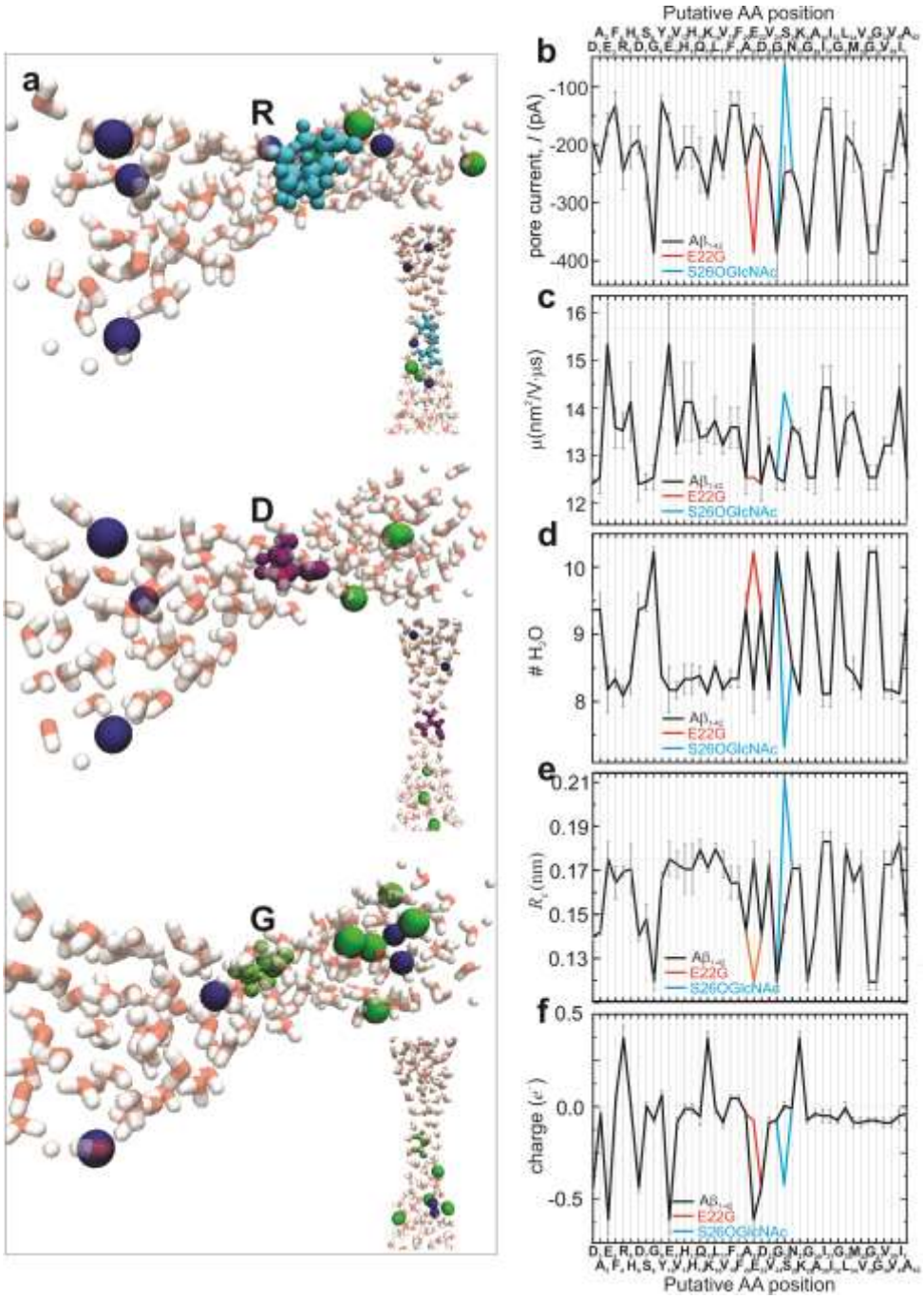
a
R
D
G
Putative AA position
b
pore current, I (pA)
c
μ(nm²/V·μs)
d
H₂O
e
Rc (nm)
f
charge (e⁻)
E22G
S26OGlcNAc
Putative AA position

FIGURE 3

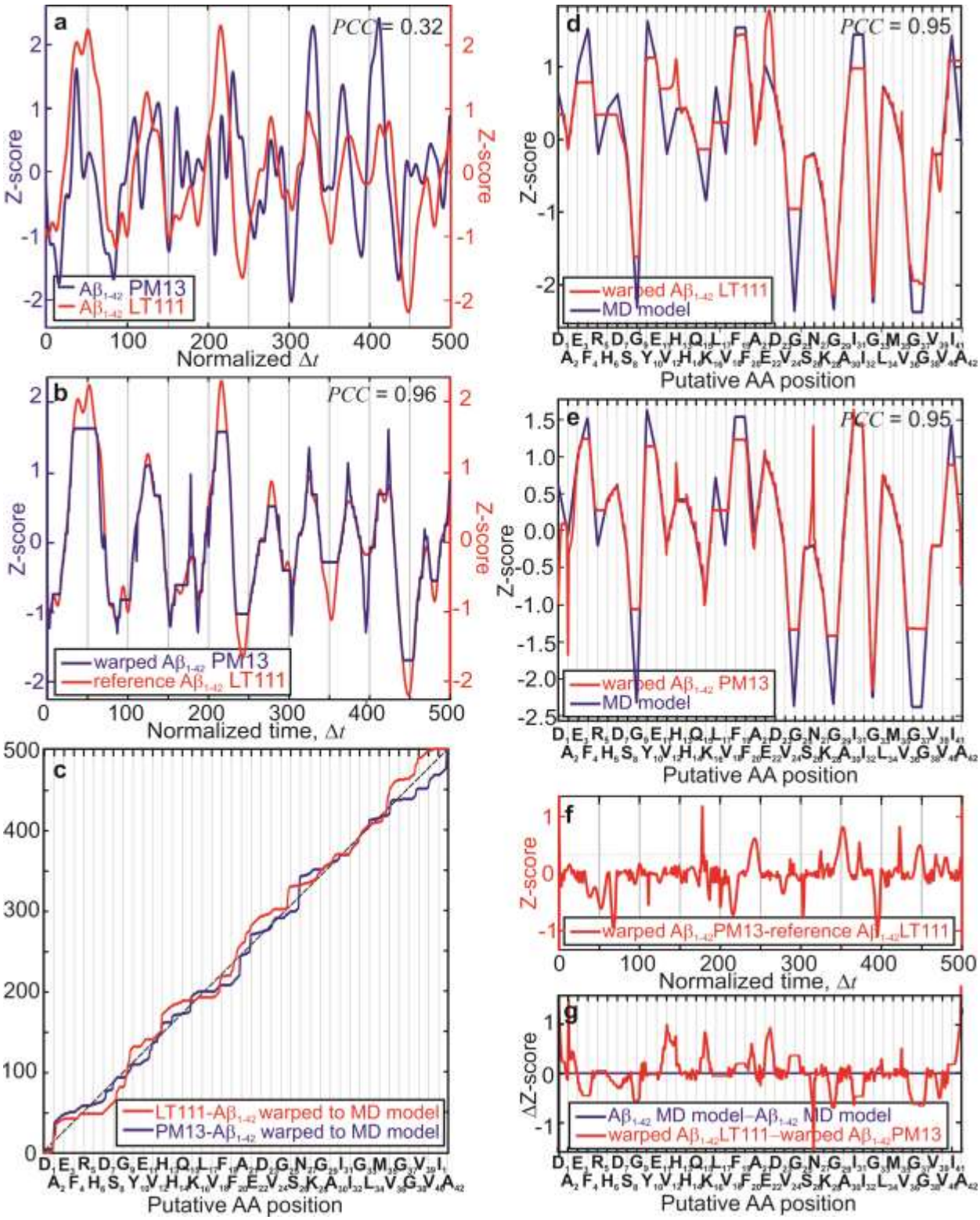
a
PCC = 0.32
Z-score
Aβ1-42 PM13
Aβ1-42 LT111
Normalized Δt
b
PCC = 0.96
warped Aβ1-42 PM13
reference Aβ1-42 LT111
Normalized time, Δt
c
LT111-Aβ1-42 warped to MD model
PM13-Aβ1-42 warped to MD model
Putative AA position
d
PCC = 0.95
warped Aβ1-42 LT111
MD model
Putative AA position
e
PCC = 0.95
warped Aβ1-42 PM13
MD model
Putative AA position
f
warped Aβ1-42PM13-reference Aβ1-42LT111
Normalized time, Δt
g
ΔZ-score
Aβ1-42 MD model–Aβ1-42 MD model
warped Aβ1-42LT111–warped Aβ1-42PM13
Putative AA position

FIGURE 4

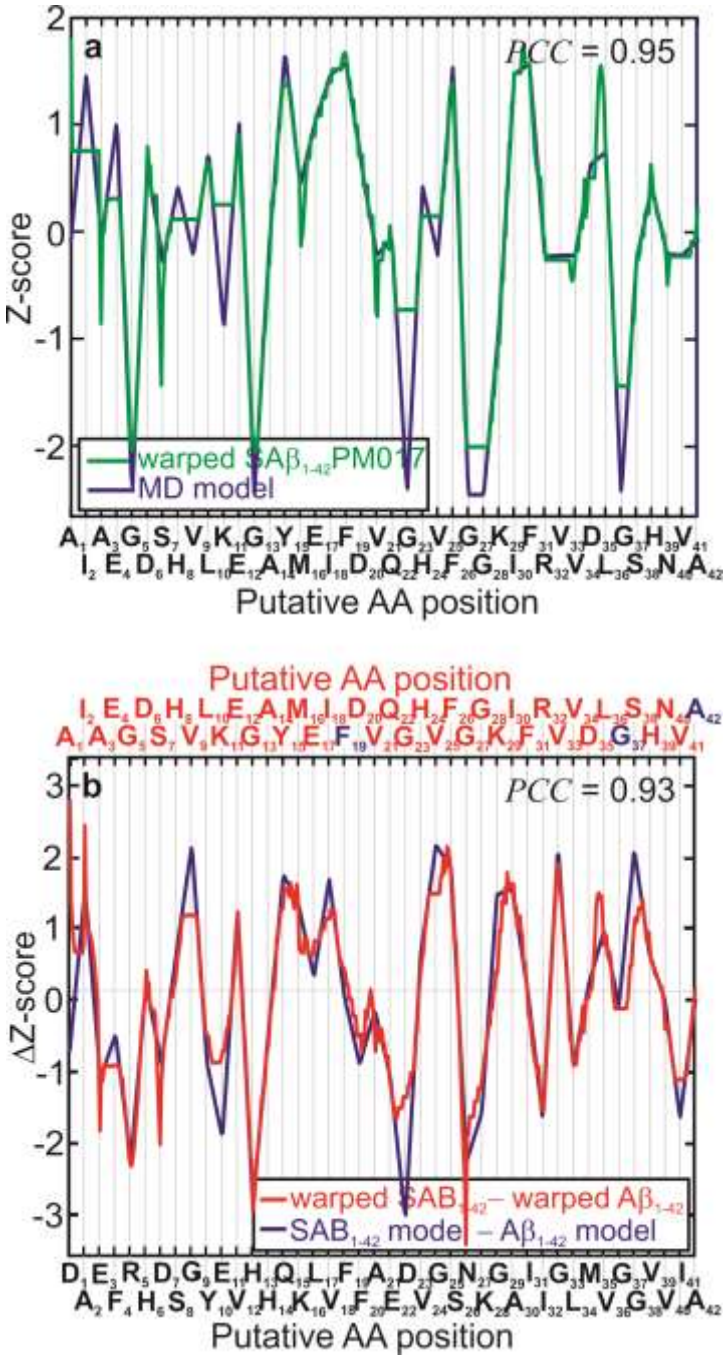
a
PCC = 0.95
Z-score
warped SAβ1-42PM017
MD model
Putative AA position
b
PCC = 0.93
ΔZ-score
warped SAB1-42 – warped Aβ1-42
SAB1-42 model – Aβ1-42 model
Putative AA position

FIGURE 5

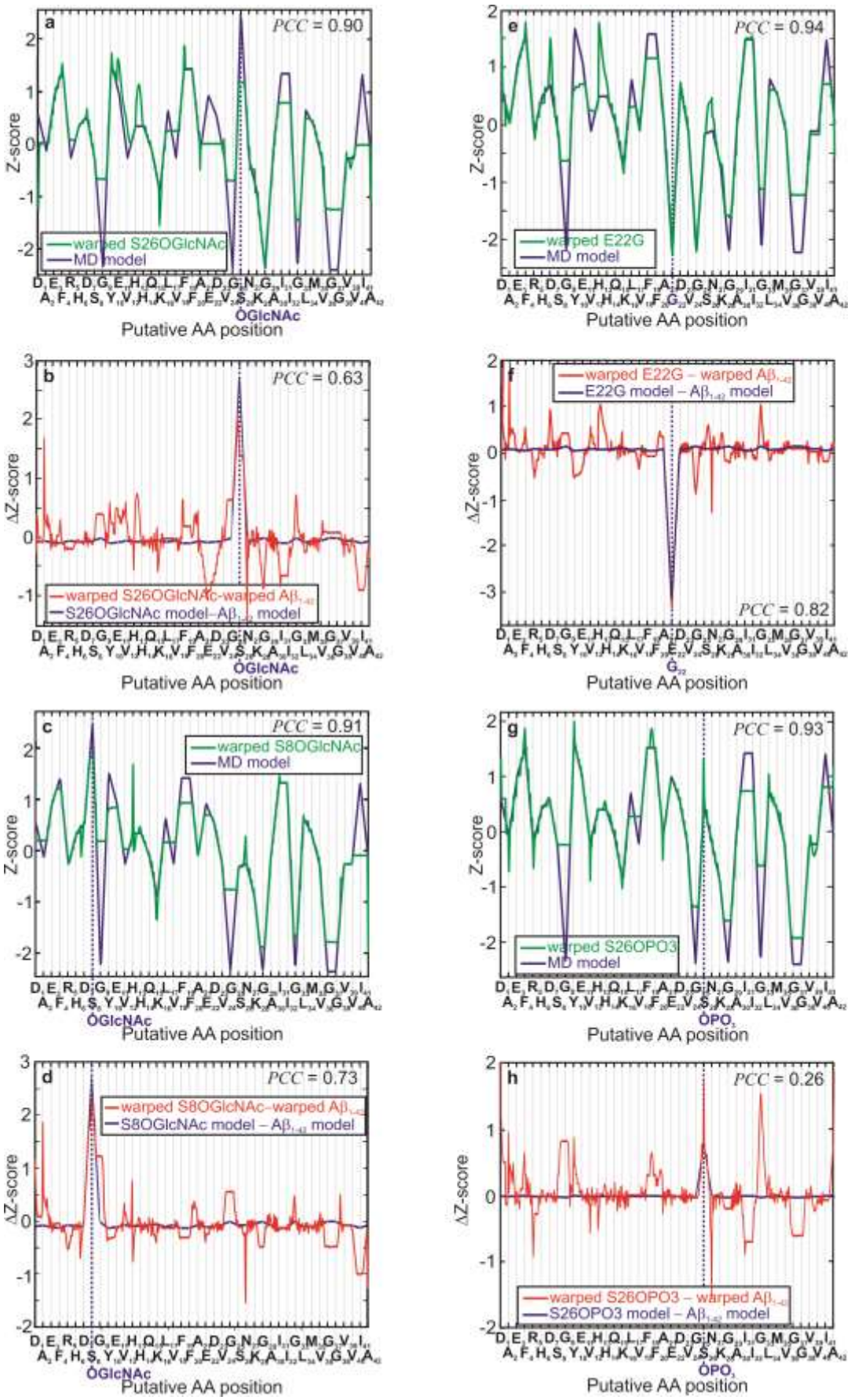
a
PCC = 0.90
Z-score
warped S26OGlcNAc
MD model
ÓGlcNAc
Putative AA position
b
PCC = 0.63
ΔZ-score
warped S26OGlcNAc-warped Aβ1-42
S26OGlcNAc model–Aβ1-42 model
ÓGlcNAc
Putative AA position
c
PCC = 0.91
Z-score
warped S8OGlcNAc
MD model
ÓGlcNAc
Putative AA position
d
PCC = 0.73
ΔZ-score
warped S8OGlcNAc–warped Aβ1-42
S8OGlcNAc model – Aβ1-42 model
ÓGlcNAc
Putative AA position
e
PCC = 0.94
Z-score
warped E22G
MD model
Putative AA position
f
warped E22G – warped Aβ1-42
E22G model – Aβ1-42 model
ΔZ-score
PCC = 0.82
Ġ22
Putative AA position
g
PCC = 0.93
Z-score
warped S26OPO3
MD model
ÓPO3
Putative AA position
h
PCC = 0.26
ΔZ-score
warped S26OPO3 – warped Aβ1-42
S26OPO3 model – Aβ1-42 model
ÓPO3
Putative AA position

(On-line) METHODS

Peptide Synthesis. The eleven carrier-free peptides used in these experiments were either purchased directly or custom-synthesized (Anaspec, Fremont, CA; Biosynthesis, Lewisville, TX) and then reconstituted according to the protocols offered by the manufacturers. To avoid aggregation, the peptides were reconstituted in a 5 nM solution with PBS without adding BSA to avoid false readings. Typically, 20 µL protein solution from a 5 nM aliquot was mixed with 50 µL of 0.1% sodium dodecyl sulfate (SDS) stock; 50 µL out of 10 mM β-mercaptoethanol (β-ME) stock; 120 µL of 500 mM *NaCl* electrolyte and 760 µL of 250 mM *NaCl* electrolyte to produce a 100 pM protein solution containing 0.005% (v/v) SDS and 500 µM β-ME in 1 mL of 250 mM *NaCl* buffer in a 1.5 mL centrifuge tube. The temperature of the tube was raised to 85°C for 2 hours to denature the protein and then the solution was cooled (to 23° C) and injected into the *cis*-reservoir of the polydimethylsiloxane (PDMS) microfluidic device bound to the silicon chip supporting the membrane with a pore through it. The *trans*-reservoir contained about 1 mL of a solution consisting of 900 µL of 250 mM *NaCl* electrolyte with 50 µL of 550 mM *NaCl* electrolyte along with 50 µL of 0.1 % (v/v) SDS.

***Sub*-nanopore fabrication and visualization.** Custom-made amorphous silicon (*a-Si*) membranes nominally 5 nm thick were manufactured (SiMPore, Inc. West Henrietta, NY) by sputter-depositing silicon on a 50 nm thick thermal SiO_2 layer grown on a float-zone silicon handle 100 µm thick, and subsequently sandwiched with another SiO_2 layer with the same 50 nm thickness followed by the deposition of 150 nm of tetraethyl orthosilicate (TEOS).[8] The TEOS was densified to decrease porosity and improve its performance as an etch mask. The *a-Si* film was sputter-deposited on a rotating substrate 25° off normal in 5-30 mTorr *Ar* gas with a large substrate-target spacing (10 cm) and low (150°C) substrate temperature. The deposition rate was

about ~0.04 nm/s. This was supposed to produce an *a-Si* film with minimal dangling-bond density and incorporated gas.

From this sandwich, membranes < 4-5 μm on-edge were revealed using an aqueous solution of ethylene diamine and pyrocatechol (EDP) chemical etch of the silicon through a silicon nitride window defined by photolithography on the polished back-side of the handle wafer. Finally, a buffered oxide etch (10:1 BOE) was used to remove the oxide. The thickness of the *a-Si* membranes, which ranged from t = 3.5 to 6 nm, was measured either by sacrificing a sister membrane fabricated similarly—puncturing it and inspecting the folded edge—or *in situ* using Electron Energy Loss Spectroscopy (EELS) on a sister chip from the same lot just prior to sputtering a pore. The roughness of the top surface of the membrane, measured with custom-built silicon cantilevers (Bruker, Fremont, CA) with 2 nm radius tips, was estimated to be < 0.5 nm-rms.

To reduce the stray capacitance, either a thick layer of photo-sensitive polyimide was spin-deposited onto the handle wafer and then patterned with UV-lithography over the membrane prior to sputtering a pore or a thick layer of polydimethylsiloxane (PDMS) with a 25 μm diameter *via* was bound to the silicon chip after sputtering a pore. To apply the polyimide, first, an adhesion promotor (Pyralin, VM-652) was spun on top of the chip for 30 sec, and then on top of that polyimide photoresist (HD8820, HD MicroSystems) was deposited at 10K rpm to produce a film thickness of 5.2±0.6 μm. After a soft-bake at 120°C for 3 min, a window the size of the membrane was opened in the resist with a 3 min UV flood exposure, followed by development in AZ 917 MIF developer and rinsed in 18 MΩ-cm de-ionized (DI) water. Subsequently, the polyimide layer was hard-baked at 250°C/300°C for 3-6 h to remove all solvents.

Just prior to loading it into the STEM column, the membranes were plasma cleaned using Tergeo-EM (PIE Scientific, Union City, CA USA). The Tergeo-EM was operated at 10 W using an 80% Ar+20% O_2 gas feed in a down-stream, pulse mode (1/16 duty-cycle, which was cycled twice for a total exposure of 2 min) such that the samples were actually outside the plasma (to eliminate sputtering) and subjected to only extremely short plasma pulses (to reduce the intensity). Subsequently, pores were sputtered through the thin *a-Si* membrane using a tightly focused, high-energy (300 kV) electron beam carrying a current ranging from 60-300 pA (post-alignment) in a (Scanning) Transmission Electron Microscope (STEM, FEI Titan 80-300 or FEI Themis Z, Hillsboro, OR) with a Field Emission Gun (FEG). Depending on the beam current and the drift, the sputtering was either timed (15 sec) or directly tracked by monitoring the Ronchigram until a pore was observed—typically, a pore opened in < 90 sec.

After sputtering, the pore was re-acquired with either High Resolution Transmission Electron Microscopy (HRTEM) or High-Angle Annular Dark Field (HAADF-)STEM. To minimize beam damage, the pores were examined using low beam current (<10–30 pA) or low voltage (80 kV) or both. The illumination convergence angle in the Titan was typically α = 10 mrad at 300kV, whereas in the Themis Z, α = 18–25 mrad at 300kV or α = 27.1 mrad at 80kV with a monochromator limiting the energy dispersion in the range 200–220 mV at 80 kV according to EELS. Whereas the Themis Z STEM resolution at 300 kV was determined to be < 60 pm on a GaN lattice, the resolution at 80 kV was < 120 pm, according to a dumbbell lattice image acquired from (110) crystalline silicon. Regardless, the high resolution probe used in HAADF-STEM facilitated the direct interpretation of the images in terms of the mass density under the beam without resorting to multiple views or simulations.

The pores through the *a*-Si membrane likely oxidize in the ambient, which might account for the change in the topography observed in Figs. 1c,d. Surprisingly, oxidation did not completely

obstruct a pore this size, possibly due to stress near the waist. It has been shown that the stress from deformation during silicon oxidation retards the reaction rate and (oxygen) diffusivity, and that the oxidation rate is generally retarded for sharp curvatures, especially at low temperature.[1-7]

Microfluidics. The silicon chip supporting the membrane with a single pore through it was bonded to a PDMS (Sylgard 184, Dow Corning) microfluidic device formed using a mold-casting technique, which has been described previously.[8,9] The PDMS microfluidic was formed from a thoroughly stirred 15:1 mixture of elastomer (siloxane) with a curing agent (cross-linker) cast in a mold formed from DSM Somos ProtoTherm 12120 plastic (Fineline Prototyping, Raleigh, NC) and then degassed and cross-linked at 75°C for 2 hrs. The microfluidic device consisted of two microchannels (each 250 × 75 μm^2 in cross-section) connected by a *via* that could be as small as 25 μm in diameter.

A tight seal was formed between the silicon chip containing the *a-Si* membrane with the pore in it and the PDMS microfluidic channel with a plasma-bonding process. First, the *cis*-channel was plasma-bonded to a clean 75 × 25 mm^2 glass slide, 1 mm-thick (VWR, Radnor, PA) using a (blue-white) 25 W oxygen (1200 sccm O_2) plasma (PDS-001, Harrick Plasma, Ithaca, NY) for 30 sec. Then, to promote adhesion and produce a hydrophilic surface while eliminating sputtering, the *Si* chip was held in vacuum, but outside the plasma, and subjected to short plasma pulses. This was accomplished using a down-stream remote plasma at 1/16 duty cycle produced in a Tergeo-EM plasma cleaner (PIE Scientific, Union City, CA USA). The Tergeo-EM was operated at 10 W with a gas feed of 10 sccm O_2 and 3 sccm *Ar*. At the same time, the PDMS microfluidic device was exposed to an oxygen (800 sccm) plasma in Harrick for 30 sec and subsequently, within 1 min the two were brought into contact under an inverted optical microscope (Axiovert-40, Zeiss) using a micromanipulator with a vacuum probe to precisely position the *Si* chip in the PDMS microfluidic. To ensure a >100 GΩ seal to the PDMS, the

backside of the silicon chip was painted with (15:1) PDMS, and then the ensemble was heat-treated at a temperature of 85°C for 24 hr in vacuum. Subsequently, *Ag/AgCl* electrodes (Warner Instruments, Hamden, CT) were embedded in each channel to independently, electrically address the *cis*- and *trans*-sides of the membrane. Supposedly, the impedance at high frequency (1 MHz) diminishes, which motivated the choice of *Ag/AgCl* electrodes.[10] The two microfluidic channels were connected to external pressure and fluid reservoirs through polyethylene tubing at the input and output ports.

Finally, to minimize electrical noise, the microfluidic chip was encased in a die-cast aluminum NEMA enclosure with coaxial electrical feed-throughs that contacted the *Ag/AgCl* electrodes immersed in the *cis*- and *trans*-reservoirs. The assays of denatured peptides were performed at 4–7°C to minimize aggregation and slow the translocation velocity.[11] This was accomplished by first refrigerating the whole assembly, i.e., the chip, microfluidic device and metallic case, to 4°C (in about 20 min) and then sandwiching it between two ice blocks for the duration of the electrical measurements.

Low-noise electrical measurements. Prior to the actual measurement, the *sub*-nanopore was first wetted by exposing the device to a remote oxygen 20 sccm, 20 W 1/16 duty-cycle for 30 sec in the Tergeo-EM plasma cleaner (PIE Scientific, Union City, CA USA). Immediately after exposure to plasma (1 min), the *cis*- and *trans*-channels in the microfluidic device were immersed in 250 mM *NaCl* electrolyte. To remove air bubbles, the microfluidic device (without protein) was also subjected to a vacuum. Subsequently, to measure the blockade current with protein in the *cis*-reservoir, a transmembrane voltage bias (< 700 mV) was applied to the reservoir relative to ground in the *trans*-channel using *Ag/AgCl* electrodes and the corresponding pore current was measured at 4–7ºC. To minimize drift and reduce acoustic noise, all the measurements were performed on an optical air table with active piezoelectric vibration control

(STACIS, TMC, Peabody, MA), housed in an acoustically isolated, NC−25 (Noise criterion) rated room in which the temperature was stabilized to less than ± 0.1 °C over 24 h through radiative cooling.

To improve the "read" accuracy, the *sub*-nanopore current was amplified with a wide-band (1.8 MHz) trans-impedance (current) amplifier (e.g., DHPCA-100, FEMTO) sampled with a DAQ at 3.6 MS/sec (PCIe-6374, NI, Austin, TX). Typically, the data were recorded continuously and filed every 15 sec (55 MS per file). Blockades were observed beyond the noise in controls that comprised the electrolyte and the denaturants (SDS and BME), which were heated to 85°C and then cooled without protein. If a pore fouled, to rehabilitate it, the microfluidic device was flushed with 18 MΩ−cm DI water for 1 da. To establish that the pore was cleared, the open pore current and current noise were measured again prior to an experiment. The pore was reused only if the noise and the open pore current returned to that observed in the pristine pore. If this procedure failed to clear it, 0.1% SDS solution was flushed through the channel to disperse latent aggregated protein in an attempt to recover the pore.

Signal recovery and reconstruction. Signal recovery and reconstruction were accomplished using customized code written in MATLAB and/or Python. There were five steps in the process: **1.** identification of blockades from a digitally filtered version of the empirical current traces; **2.** selection of a workable subset from the unfiltered empirical data and then uniformly sampling and re-scaling each event; **3.** digitally filtering and identifying those blockades with similar fluctuation patterns recursively using an affinity propagation algorithm to produce tight clusters; **4.** identifying reverse-time clusters using the dynamic time warping algorithm (DTW) distance between clusters; and finally, and finally, **5.** aligning the empirical consensus with a MD model using a DTW algorithm.

1. First, events were detected from empirical current traces subjected to a low-pass, 8-pole Bessel filter with a 20 kHz cutoff frequency using *OpenNanopore*[12] with an S = 3.8 deviation from the baseline and end at E = 0 from the baseline with a filter coefficient F = 0.999 and 10 baseline points included for the CUSUM–fit. Events that qualified as blockades satisfied the criteria that the open pore current $I_0 \geq 150$ pA with I_0 after the event was within 10 pA of the open pore current prior to the event. The events that qualified as blockades were subsequently extracted from the unfiltered empirical data, along with a header and footer 200 samples long, which extended beyond the duration of the blockade so that to any artifacts associated with filtering would be divorced from the signal. The blockade, ΔI, the (local) open pore current, I_0, and blockade duration, Δt, were calculated for each event using data filtered through an 8 pole low pass Bessel filter. Typically, the number of blockades detected in a single experiment ranged between 2000 and 5000.

2. A subset of the empirical data was selected by culling blockades with a duration too short to satisfy the Nyquist criterion or too long to preclude back-stepping. Likewise, blockades with a fractional blockade current, $\Delta I/I_0$, beyond the 50% contour (Fig. 1g, red highlight) were also culled. Three subsets were compiled by zero-phase-shift filtering each blockade with 5th order low-pass Butterworth IIR filter with a pass-band defined by the 3dB point at (the low frequency) 17-cycles/(½ blockade duration) and (the high frequency) 42-cycles/(½ blockade duration), and with a 5th order pass band Butterworth IIR filter with defined by the 3dB points at 1.5-cycles/(½blockade duration) and 42-cycles/(½blockade duration). The 200-point headers and footers were removed after filtering. Since the durations were variable, the number of samples in each blockade also varied.[13-16] So, each of the selected blockades were re-sampled to a normalized time-scale with 500 samples. Finally, since the blockade current varied (within 10%

of I_0), the mean current was zeroed and the result normalized by the standard deviation (σ) to form the Z-score or the standard score for each blockade.

3. The selected, renormalized blockades were subsequently recursively clustered using an affinity propagation (AP) algorithm implemented in MATLAB (apcluster.m) to identify blockades with similar fluctuation patterns. First, a subset filtered at 17 cycles was used to compute the blockade cross-correlation distance matrix. Based on distance matrix, AP grouped blockades into clusters. Indices of clustered blockades were then used to assemble consensuses from the subset filtered at 42 cycles. The cross-correlation distance matrix was computed for clusters consensuses and passed to AP algorithm. AP grouped similar clusters into a super-cluster.

4. To form a consensus, super-clusters with the shortest mean Euclidean distance between the filtered elements or the shortest median duration were selected. A second super-cluster was then identified by the shortest DTW distance to the time-reversed version of the first. The elements of the latter super-cluster were time-reversed and combined into final consensus. The resulting consensus terminals were trimmed (typically by 5 points) and then resampled to 500 points.

5. Finally, DTW was used to align the time-axis of the consensus to a volume model and call the acids from the blockade current fluctuations. The DTW algorithm implemented in Python can be found on-line at: https://github.com/statefb/dtwalign.[17] DTW computes the local stretch or compression to apply to the time axes of two time-series in order to optimally map one (query) onto the other (reference). The signal associated with each peptide was modeled by represented each acid in the peptide sequence by the current derived from molecular dynamics simulations.

Finite Element Simulations (FES). The finite element simulations (FESs) were performed by using COMSOL (v5.6, COMSOL Inc., Palo Alto, CA, USA) as described elsewhere.[8,9] Tersely, the FESs were based on continuum modeling, which accounted for a bi-conical shape of the

particular pore, the reduced electrophoretic mobility and the steric effect of ions explicitly.[9] The electrohydrodynamics was governed by coupled Poisson and Stokes equations. Briefly, the applied potential φ and the potential ψ due to charges in the pore were de-coupled from one another and solved independently. The relationship between ϕ and the charge carriers, e.g. Na^+ and Cl^-, is given by the Poisson equation, $\nabla^2\psi = -\rho / \varepsilon\varepsilon_0$, where ρ, ε and ε_0 were the volume charge density and the relative and vacuum permittivities, respectively. The charge density is given by $\rho = F\sum_i z_i c_i$ where F = 96,485 C mol^{-1} is the Faraday constant, z_i is the valence and c_i is the molar concentrations of ith ionic species in the bulk. Electro-osmotic flow was captured by the Navier–Stokes equation: i.e. $\eta\nabla^2 u - \nabla p - F\sum_i z_i c_i \nabla V = 0,$ where the total potential, V = φ + ψ, η is the viscosity, p is the pressure and u is the velocity vector. The transport of ionic species is described by the Nernst–Planck equation given by: $D_i\nabla^2 c_i + z_i\mu_i c_i \nabla^2 V = u \cdot \nabla c_i,$ where D_i is the diffusion coefficient and μ_i is the ionic mobility of the ith species. Thus, u, V and c_i are coupled between equations. The boundary conditions are specified in the Supplemental Table 3 and material properties such as the diffusivity in the *sub*-nanopore were restricted by the literature as elaborated elsewhere.[9]

Following other work,[9] to estimate the pore conductance the radial distributions of the electric potentials and ion concentrations were calculated, assuming that the radius-dependent concentration followed a Boltzmann distribution according to: $\nabla^2\Psi = \sinh(\Psi)/\lambda^2(1+\alpha(\cosh(\Psi)-1))$, $\Psi = e\psi / k_B T$ where ψ is the (radius-dependent electric potential), k_B is the Boltzmann constant; T is the absolute temperature; and l is the Debye screening length and $\alpha = 2a^3 n_0$, where a is the radius of the solvated ion. The topography of each pore was taken into account to match the data. With the assumption of a pore topography, the effective thickness of the membrane was estimated from the electric field distribution using

FESs. With this estimate, the surface charge density was then inferred from measurements of the pore conductance at dilute concentration, assuming initially that the cations carried the current prodominately and negligible electro-osmotic flow.

Molecular Dynamics (MD) Simulations. For an accurate assessment with atomic detail, following earlier work,[18] the ion and peptide transport was simulated in a *sub*-nanopore through a silica membrane by MD. All simulations were performed using NAMD version 2.14 in NVT ensemble.[19] To construct the *sub*-nanopore, initially, a crystalline silica slab was generated with a number of unit cells required to fill the pore-excluded volume of the amorphous silica (SiO_2) membrane with a density of 3.0 g/cm^3. The surface geometry of a double conical *sub*-nanopore having an elliptical cross-section was modeled using the relation:

$$\sqrt{x^2 + y^2} < (d_0 / 2) + |z| \tan(\gamma) + \delta$$

where $\gamma = 10°$ is the cone angle at the minimum cross-section of the *sub*-nanopore near the waist, $d_0 = 0.4$ *nm* is the diameter of the pore at the waist and δ is the van der Waals radii of the pore surface atoms (taken as 0.16 nm). The *Si* and *O* atoms were randomly placed inside the membrane, excluding the volume of the *sub*-nanopore, and then the entire membrane was subjected to simulated annealing at a high temperature 7000 K. A repulsive grid potential was applied to avoid the entry of SiO_2 atoms inside the *sub*-nanopore and CHARMM force field parameters were used for *Si* and *O* atoms in the membrane.[21] Later, the bonds between the *Si* and *O* atoms of silica were defined using a 0.22 nm distance cut-off. Using this protocol, a silica *sub*-nanopore with a diameter of 0.4 nm was created, similar to the actual topography (Fig. 1d). A similar protocol was successively used to obtain the stable silica pores in previous studies.[20-23] In the process of creating the pore, the resulting total charge of the membrane was typically non-zero so, to maintain the electro-neutrality, the partial charges on the *Si* atoms were adjusted so that the total charge of the membrane was zero.

The MD simulations were performed for the β-amyloid peptide and fragments of it translocating through the pore spanning the membrane. The coordinates for β-amyloid (pdbcode:1IYT) peptide were obtained from the protein data bank (PDB);[24] the peptide fragments of it were constructed from VMD using CHARMM36[26] topologies and force-fields. The glycosylated serine variant with O-linked β-N-acetylaglucosamine (O-GlcNAc) was constructed using CHARMM-GUI.[25] The constructed peptide structures were placed at the orifice of the pore to study their translocations through the entire silica *sub*-nanopore and CHARMM36 force field parameters were employed for the peptide fragments.[26] The constructed silica *sub*-nanopore-protein complex was solvated with a 5 nm thick TIP3P water film on either side of the pore to screen the electrostatic interactions of the pore with its periodic images.[27] The Na^+ and Cl^- counter ions were added to the solvated pore to set 200 mM *NaCl* concentration. Initial systems were subjected to 2000 steps of conjugate-gradient minimization to remove the bad contacts and followed by 1 ns NPT equilibration at temperature 300 K with a 1 fs time step for integration to achieve the bulk water density to 1.0 g/cm^3. Periodic boundary conditions were used in all three directions.

A Nosé–Hoover thermostat with a damping coefficient of 1 ps was connected to silica atoms of the membrane to maintain the temperature.[28] Subsequently, the equilibrated systems were subjected to a 20 ns NVT MD simulation with a 0.12 nm cutoff for calculating the short-range part of the non-bonding interactions and the long-range electrostatic interactions were calculated using Particle-Mesh-Ewald (PME) method.[29]

To simulate the translocation of a peptide, the molecular force fields describing water, ions, and the peptide were combined with the CHARMM force fields for the SiO_2 in a 5 nm thick membrane. To mimic the experiments, the membrane separated an aqueous solution of *NaCl* into two compartments connected by the bi-conical *sub*-nanopore. A 5 V potential drop was applied

across the membrane spanned by the *sub*-nanopore system for each of the peptide fragments to induce the ionic flux and subsequently, the fragments were impelled through the pore by pulling with a zero-acceleration velocity of 5×10^{-6} *nm/ps*. The travel of the fragment was determined by a combination of both the electric force and the velocity, but the velocity made a larger contribution. The movement of the ions was determined by the electric force.

The ionic current inside the *sub*-nanopore was computed using:

$$I(t) = \frac{1}{\Delta t \cdot L_z} \sum_{i=1}^{N} q_i [z_i(t+\Delta t) - z_i(t)]$$

where z_i and q_i are the *z*-coordinate and atomic charge of the ith ion, respectively. The parameter *N* represents the total number of ions present in the pore and L_z represents the *z*-dimension of the system (14 *nm*). The pore current, AA mobility, hydration, charge and gyration radii, R_g, at the minimum cross-section of the pore are computed using the peptide translocation trajectories and then the data for the entire β-amyloid peptide and its variants, E22G and S26GlcNAc, were constructed and arranged according to the sequence of β-amyloid. An acid was taken to be within the pore waist when -0.3 nm < *z* < 0.3 nm, with the origin at 0, which demarcates the region of interest. All the data, including the current, were collected when the fragments were in this *z*-range.

Force and Pore Current Molecular Spectroscopy with an Atomic Force Microscope (AFM). The force and current data were acquired from single protein molecules using a customized AFM (MFP-3D-BIO, Asylum Research, Santa Barbara, CA) interfaced to an inverted optical microscope (Axio-Observer Z1, Zeiss), all enclosed within a Faraday cage, as described elsewhere.[30] Tersely, a low noise Z-sensor in the AFM was coupled with an ultra-quiet Z-drive to produce noise in the tip-sample distance < 30 pm at 1 kHz bandwidth. To minimize drift and reduce acoustic noise, an inverted optical microscope was mounted on an optical air table with active piezoelectric vibration control (Stacis, TMC, Peabody, MA), housed in an

acoustically isolated, NC-25 (Noise criterion) rated room in which the temperature was stabilized to less than ± 0.1 °C over 24 h through radiative cooling. Temperature fluctuations appeared to be a source of long-term drift but with temperature regulation, the drift of the system was reduced to 0.6 nm/min. Sound couples strongly into the microscope and was another potential source of instrument noise. Therefore, acoustically loud devices, especially those with cooling fans such as power supplies, amplifiers, and computers, were placed outside of the room. With these precautions, force detector noise is < 10 pm/√Hz for frequencies above 1 Hz; the on-surface positional noise measured < 45 pm A-dev.

To acquire the data, first, the topography of the membrane and the location of the pore relative to the edges of the membrane were determined in air in non-contact (tapping) mode using a silicon cantilever (SSS-FM, Nanosensors, Neuchatel, Switzerland) with a 2 nm nominal radius, and a spring constant ranging from K_{spr} = 0.5-9.5 nN/nm and a 45-115 kHz resonant frequency (in air). Force spectroscopy was performed in a 250 mM *NaCl* electrolytic solution, using a custom MSNL silicon cantilever (Bruker, Camarillo, CA) without metal reflex with a 2 nm tip radius. Each MSNL probe includes six cantilevers with a range of force constants (10 < K_{spr} < 100 pN/nm) and resonant frequencies (7< ω_0 <125 kHz). Considering only the off-resonance thermal noise of the cantilever $\Delta F_{\min} = \sqrt{4k_B T \Delta f K_{spr} / \omega_0 Q} < 1pN$, where typically K_{spr} ~ 10-30 pN/nm, Δf = 100-3300 Hz was the measurement bandwidth, $\omega_0 = 2\pi\times5.3$ -18 kHz was the angular resonance frequency of the cantilever, and Q ~15-17(0.8-1.3) was the quality factor in air (liquid).

To locate the pore relative to fiducial marks, i.e., the edges of the (4 × 6 μm^2) membrane, an AFM topographical scan was performed with a sharp tip in liquid in constant force (contact) mode. After that, the pore location was re-acquired in liquid with a second cantilever on the same probe through triangulation from the fiducial marks and a small area scan. Then a constant

+0.70 V was applied to the anode on the *trans*-side of the membrane with the cathode on the *cis*-side grounded, and the pore current was measured continuously with an external amplifier, while the force on the cantilever was determined from the deflection. Starting from a position about 100-120 nm above the membrane, the tethered protein, immersed in a solution of 250 mM *NaCl* electrolyte and SDS, was repeatedly advanced towards the sub-nanopore at 20 nm/s, captured and threaded through it by the electric field, and then retracted from it at a constant 4 nm/s velocity by the AFM while the current, tip deflection and Z-position were recorded. The tip position above the membrane was determined from the sum of the tip deflection and Z-sensor position.

The ionic current through a nanopore was measured in a Faraday cage with a patch-clamp amplifier (Axopatch 200B, Molecular Devices) in whole-cell mode. *Ag/AgCl* electrodes embedded in the microfluidic device were used to establish a transmembrane potential. An electrical bias of +0.70 V was applied between *Ag/AgCl* electrodes embedded in the *trans*- and *cis*-channels, respectively, and the current between them was measured using an Axopatch 200B amplifier at 17.6 ± 0.1 °C. Each data channel was subsequently digitally filtered at 5 kHz and sampled at 10 kHz and then digitally filtered again using a 100 Hz eight-pole Bessel filter (MATLAB, 2016a).

REFERENCES FOR THE METHODS

1. Zhang, M., Schmidt, T., Sangghaleh, F., Roxhed, N., Sychugov, I. & Linnros, J. Oxidation of nanopores in a silicon membrane: self-limiting formation of sub-10 nm circular openings. *Nanotechnology*, **25**(35), 355302 (2014).
2. Kao, D-B., McVittie, J.P., Nix, W.D. & Saraswat, K.C. Two-Dimensional Thermal Oxidation of Silicon—I. Experiments. *IEEE Trans. Electron Dev.* **ED-35,** 25-37 (1988).

3. Han, X-L., Larrieu, G. & Krzeminski, C. Modeling and engineering of stress-based controlled oxidation effects for silicon nanostructure patterning. *Nanotechnology* **24**, 495301 (2013).

4. Khalilov, U., Pourtois, G., van Duin, A.C.T. & Neyts, E.C. Self-Limiting Oxidation in Small-Diameter Si Nanowires. *Chem. Mater.* **24,** 2141-2147 (2012).

5. Morita, M.; Ohmi, E.; Hasegawa, E.; Kawakami, M.; Suma, K. Control factor of native oxide growth on silicon in air or in ultra-pure water. *Appl. Phys. Lett.* **55**(6), 562-564 (1989).

6. Fritzshe, H.; Tsai, C.C. Porosity and Oxidation of Amorphous Silicon films Prepared by Evaporation, Sputtering and Plasma-Deposition. *Solar Energy Materials* **1**, 471-479 (1979).

7. Ohsaki, H.; Miura, K.; Tatsumi, Y.; Ino, T. Structure of the Natural Oxide of Amorphous Silicon. Jap. *J. Appl. Phys.* **25**(12) 1773-1777 (1986).

8. Liu, X., Dong, Z & Timp, G. Calling the amino acid sequence of a protein/peptide from the nanospectrum produced by a sub-nanometer diameter pore. *Scientific Reports,* **12,** 17853 (2022).

9. Rigo, E., Dong, Z., Park, J.H., Kennedy, E., Hokmabadi, M., Almonte-Garcia, L., Ding, L., Aluru, N. & Timp, G. Measurements of the Size and Correlations between Ions using an Electrolytic Point Contact. *Nat. Commun.,* **10,** 2382 (2019) https://doi.org/10.1038/s41467-019-10265-2.

10. Xu, S. Dai, M., Xu, C., Chen, C., Tang, M., Shi, X. & Dong, X. Performance Evaluation of Five Types of Ag/AgCl Bio-Electrodes for Cerebral Electrical Impedance Tomography. *Ann. Biomed Eng.* **39**(7), 2059-2067 (2011).

11. Ortiz-Young, D., Chiu, H.C., Kim, S., Voïtchovsky, K. & Riedo, E. The interplay between apparent viscosity and wettability in nanoconfined water. *Nature Comm.,* **4,** 2482 (2013).

12. Raillon, C., Granjon, P., Graf, M., Steinbocka, L.J. & Radenovic, A. Fast and automatic processing of multi-level events in nanopore translocation experiments. *Nanoscale*, 4, 4916-4924 (2012).

13. Fay, G. & Kang, S. Average sampling of band-limited stochastic processes. *Appl. Comp. Harmonic Anal.*, **35**, 527-534 (2013).

14. Long, D.G. & Franz, R.O.W. Band-Limited Signal Reconstruction from Irregular Samples with Variable Apertures. *IEEE Trans. Geosci. Remote Sens.,* **54**(4), 2424-2436 (2016).

15. Wang, D., Liu, X., Wu, X. & Wang, Z. Reconstruction of Periodic Band Limited Signals from Non-Uniform Samples with Sub-Nyquist Sampling rate. *Sensors*, **20**, 6246 (2020).

16. Margolis, E. & Eldar, Y.C. Nonuniform Sampling of Periodic Bandlimited Signals. *IEEE Trans. Signal Process.,* **56**(7), 2728-2745 (2008).

17. Giorgino, T., Computing and Visualizing Dynamic Time Warping Alignments in R: The dtw Package. *J. Stat. Soft.,* **31** (2009) doi:10.18637/jss.v031.i07.

18. Phillips, J.C., Braun, R., Wang, W., Gumbart, J. Tajkhorshid, E., Villa, E., Chipot, C.; Skeel, R. D., Kale, L., Schulten, K., Scalable Molecular Dynamics with NAMD. *J. Computational Chem.*, **26,** 1781-1802 (2005).

19. Cruz-Chu, E.R., Aksimentiev, A. & Schulten, K. Water-Silica Force Field for Simulating Nanodevices. *J. Phys. Chem. B,* **110**, 21497-21508 (2006).

20. Aksimentiev, A., Brunner, R.K., Cruz-Chu, E., Comer, J. & Schulten, K. Modeling Transport through Synthetic Nanopores. *IEEE Nanotechnol.,* **3**, 20-28 (2009).

21. Vollmayr, K., Kob, W. & Binder, K. Cooling-Rate Effects in Amorphous Silica: A Computer-Simulation Study. *Phys. Rev. B,* **54**, 15808 (1996).

22. Humphrey, W., Dalke, A. & Schulten, K. VMD: visual molecular dynamics. *Journal of molecular graphics* **14**, 33-38 (1996).

23. Cruz-Chu, E.R., Aksimentiev, A. & Schulten, K. Ionic Current Rectification through Silica Nanopores. *J. Phys. Chem. C,* **113**, 1850-1862 (2009).

24. Crescenzi, O., Tomaselli, S., Guerrini, R., Salvadori, S., D'Ursi, A.M., Temussi, P.A. & Picone, D. Solution Structure of the Alzheimer Amyloid β-Peptide (1–42) in an Apolar Microenvironment: Similarity with a Virus Fusion Domain. *European J. Biochem.*, **269**, 5642-5648 (2002).

25. Jo, S., Kim, T., Iyer, V.G. & Im, W. CHARMM-GUI: A Web-Based Graphical User Interface for Charmm. *J. Computat. Chem.,* **29**, 1859-1865 (2008).

26. Best, R.B., Zhu, X., Shim, J., Lopes, P. E., Mittal, J., Feig, M. & MacKerell Jr., A.D., Optimization of the Additive Charmm All-Atom Protein Force Field Targeting Improved Sampling of the Backbone ϕ, Ψ and Side-Chain X1 and X2 Dihedral Angles. *J. Chem. Theor. Computat.,* **8**, 3257-3273 (2012).

27. Price, D.J. & Brooks III, C.L. A Modified TiP3P Water Potential for Simulation with Ewald Summation. *J. Chem. Phys.,* **121**, 10096-10103 (2004).

28. Evans, D.J. & Holian, B.L. The Nose–Hoover Thermostat. *J. Chem. Phys.,* **83**, 4069-4074 (1985).

29. Darden, T., York, D. & Pedersen, L. Particle Mesh Ewald: An N· Log (N) Method for Ewald Sums in Large Systems. *J. Chem. Phys.,* **98**, 10089-10092 (1993).

30. Dong, Z., Kennedy, E. & Timp, G. Discriminating Residue Substitutions in a Single Protein Molecule Using a Sub-nanopore. *ACS Nano* **11**(6), 5440-5452 (2017).

SUPPLEMENTAL MATERIALS for

De-coding Proteoforms with Single Acid Resolution Using a Sub-nanometer Diameter Pore

Tautvydas Lisauskas,[1#] *Archith Rayabharam,*[2#] *Punam Murkute,*[1]*Lisa Almonte,*[1] *Eveline Rigo,*[1] *Juan Oviedo Robles,*[1] *Zhuxin Dong,*[1] *Joshy Joseph,*[1] *Narayana Aluru,*[2] *and Gregory Timp*[1]*
[1]Electrical Engineering and Biological Science, University of Notre Dame, Notre Dame, IN 46556 USA
[2]Department of Mechanical Engineering, University of Texas, Austin, TX 78712-1229 USA

SUPPLEMENTAL TABLE 1. Amino acid (AA) residue volumes used in the peptide analysis. The AA and glucosamine volumes were taken from the averages reported in: [P] Perkins, S.J. Protein volumes and hydration effects. *Eur. J. Biochem.* **157,** 169–180 (1986). These averages were generally consistent with those in: [Z] Zamyatnin, A.A. Protein volume in solution. *Prog. Biophys. Mol. Biol.*, **24**,107-123 (1972); and [T] Tsia, J., Taylor, R., Chothia, C. & Gerstein, M. The Packing Density in Proteins: Standard Radii and Volumes, *J. Mol. Biol.*, **290,** 253-266 (1999). The hydropathy ranking 1-20 was taken from [B] Bonella, S., Raimondo, D., Milanetti, E., Tramontano, A. & Ciccotti, G. Mapping the Hydropathy of Amino Acids Based on Their Local Solvation Structure. *J. Phys. Chem. B.* **118,** 6604-6613 (2014). For comparison, the hydropathy indices is also shown from [K] Kyte, J. & Doolittle, R.F. A simple method for displaying the hydropathic character of a protein. *J. Mol. Biol.* **157,** 105-132 (1982).

Amino acid	**Abbreviation**	**Molecular mass (Da)**	**# of atoms**	**MD pore current (pA)**	**Volume (nm^3)** [P]/[Z]/[T]	**Hydropathy** [B]/[K]
Alanine	A	89	13	236.2 ± 11.2	0.0878/0.0886/0.0901	13/1.6
Arginine	R	174	26	245.8 ± 30.5	0.1882/0.1734/0.1928	3/-12.3
Asparagine	N	132	17	244.4 ± 6.8	0.1201/0.1141/0.1275	1/-4.8
Aspartic acid	D	133	16	191.5 ± 24.1	0.1154/0.1111/0.1171	8/-9.2
Cysteine	C	121	14	232.2 ± 3.9	0.1054/0.1085/0.1035	12/2
Glutamine	Q	146	20	234.9 ± 47.0	0.1451/0.1438/0.1494	7/-4.1
Glutamic Acid	E	147	19	165.2 ± 19.3	0.1409/0.1384/0.1408	6/-8.2
Glycine	G	75	10	386.9 ± 47.9	0.0599/0.0601/0.0638	14/1
Histidine	H	155	20	204.5 ± 35.2	0.1563/0.1532/0.1593	2/-3
Isoleucine	I	131	22	137.9 ± 18.5	0.1661/0.1667/0.1649	19/3.1
Leucine	L	131	22	183.9 ± 42.1	0.168/0.1667/0.1646	20/2.8
Lysine	K	146	24	289.0 ± 4.5	0.1727/0.1686/0.1700	4/-8.8
Methionine	M	149	20	203.6 ± 42.6	0.1652/0.1629/0.1677	16/3.4
Phenylalanine	F	165	23	131.6 ± 22.9	0.1897/0.1899/0.1935	15/3.7
Proline	P	115	17	178.7 ± 23.2	0.1233/0.1127/0.1231	17/-0.2
Serine	S	105	14	248.7 ± 45.7	0.0917/0.089/0.0942	5/0.6
Threonine	T	119	17	251.8 ± 53.8	0.1183/0.1161/0.1200	9/1.2
Tryptophan	W	204	27	131.3 ± 29.3	0.2279/0.2278/0.2317	11/1.2
Tyrosine	Y	181	24	124.2 ± 9.9	0.1912/0.1936/0.1971	10/-0.7
Valine	V	117	19	245.2 ± 12.0	0.1388/0.140/0.1391	18/2.6
water	H_2O	18	3		0.0245/0.0297	
PO_4^{3-}	PO_4^{3-}	95/79.97	5		0.0565	
glucosamine	GlcNAc	221.21	30		0.222.0±0.002	

SUPPLEMENTAL TABLE 2. Sequences of amyloid-beta ($A\beta_{1-42}$) and variants of it. The blue symbols indicate the substitutions/mutations sites in $A\beta_{1-42}$ whereas the red letters indicate the acids sites in common with $A\beta_{1-42}$.

$A\beta_{1-42}$	*DAEFRHDSGYEVHHQKLVFFAEDVGSNKGAIIGLMVGGVVIA*
$SA\beta_{1-42}$	*AIAEGDSHVLKEGAYMEI**F**DVQGHVF**G**GKIFRVVDLGSHNV**A***
S26OGlcNAc	*DAEFRHDSGYEVHHQKLVFFAEDVG-**S(OGlcNAc)**-NKGAIIGLMVGGVVIA*
S8OGlcNAc	*DAEFRHD-**S(OGlcNAc)**-GYEVHHQKLVFFAEDVGSNKGAIIGLMVGGVVIA*
E22G	*DAEFRHDSGYEVHHQKLVFFA**G**DVGSNKGAIIGLMVGGVVIA*
S26OPO3	*DAEFRHDSGYEVHHQKLVFFAEDVG-**S(O-PO$_3$)-**NKGAIIGLMVGGVVIA*
F4W	*DAE**W**RHDSGYEVHHQKLVFFAEDVGSNKGAIIGLMVGGVVIA*
F20C	*DAEFRHDSGYEVHHQKLVF**C**AEDVGSNKGAIIGLMVGGVVIA*

SUPPLEMENTAL NOTE #1: The electric field and current in a *sub*-nanopore.

The precision with which *sub*-nanometer-diameter pores were fabricated translated directly to very stringent control of the electric field and current distribution. Finite element simulations (FESs) of the electric field and the electro-osmotic flow were performed using COMSOL (v5.6, COMSOL Inc., Palo Alto, CA), following a modified Poisson-Boltzmann formalism described in: Rigo, E., et al. Measurements of the Size and Correlations between Ions using an Electrolytic Point Contact. *Nat. Commun.*, **10,** 2382 (2019).

For the simulations, a conformal layer of amorphous silicon dioxide (SiO_2) membrane covering an amorphous silicon (a-*Si*) membrane was constructed with a bi-conical pore through it with a *sub*-nanometer-diameter waist. The cone angle ranged from 5-15° near the waist, but expanded to 25-40° near the orifice of the pore. It was assumed that the pore was immersed in 250 mM *NaCl* and a transmembrane bias voltage was applied across the membrane. The boundary conditions for the system are given in supplemental Table 3. The thin (3.5-6 nm) membranes, in conjunction with the bi-conical topography, tightly focused the electric field along the pore axis as evident in supplemental Fig. 1, for L_m = 5 nm with a bias voltage of 0.6 V. Thus, the potential (and the electric force) in a pore was confined to 0.70 nm region near the constriction (full width-half maximum), which corresponds to about 1–2 AAs in a linear peptide

chain assuming that the spacing between α-carbons is about 0.38 nm (supplemental Fig. 1b). Support for these assessments of the potential was obtained from measurements of the open pore current-voltage characteristics of *sub*-nanopores. Typical current-voltage characteristics are shown in supplemental Fig. 1. They were approximately linear over a range of ± 1V. A line-fit to this data yielded a conductance of 330 pS for a 0.4 nm-diameter in 250 M *NaCl*. The concentration dependence of the conductivity suggests that there is a fixed charge in the pore (in this case $\sigma = -0.05\ e/nm^2$). Accounting for the surface charge, finite element simulations (FES) can reproduce quantitatively the measured conductance (red dashed line, supplemental Fig. 1c).

SUPPLEMENTAL TABLE 3: Simulation Parameters.

Feature	Boundary Conditions
1. *sub*-nanopore	d = 0.4 *nm* diameter, L_m = 5 *nm thick* 10° bi-conical structure
2. *a-Si* membrane	t_{Si} = 5 *nm*; ε_r = 11.7
3. SiO_2 membrane	t_{ox} = 1 *nm* thick, $\sigma = -0.05\ e/nm^2$; ε_r = 3.9
4. Electrolyte	250 mM *NaCl*; ε_r=78.5; η = 1.002 mPa·s; D_{Na} =0.07×1.33×10^{-9} m^2/s; D_{Cl} = 0.007×2.03×10^{-9} m^2/s.
5. zeta-potential, ζ; ionic radius, a, and α	$\zeta = -0.007\ V$; a = 0.15 nm ; α = 0.0010162

SUPPLEMENTAL FIGURE 1

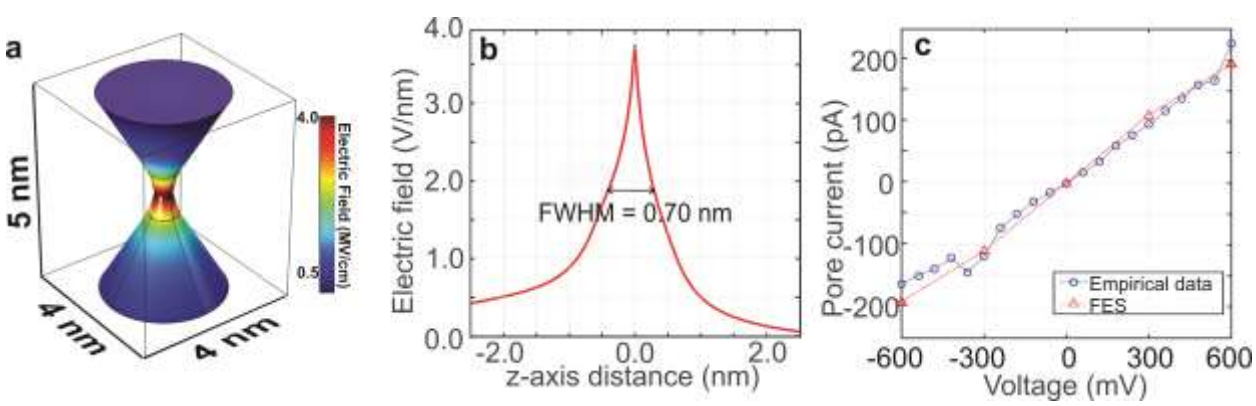

SUPPLEMENTAL FIGURE 1. Finite Element Simulation (FES) of a *sub*-nanopore. (a) Based on the *sub*-nanopore topography inferred from HAADF-STEM after oxidation, a three-

dimensional (3D) model was used to estimate the electric field distribution along the pore (*z*-) axis. What's shown is a schematic representation of a *sub*-nanopore through a 5 nm thick membrane with a bi-conical topography that is 0.4 nm diameter at the waist with a 10° cone-angle that opens to 30°. **(b)** An FES of the electric field distribution in the pore is shown. The full-width at half-maximum (FWHM) of the electric field distribution is 0.70 nm. **(c)** A measurement of the current-voltage characteristics of an actual *sub*-nanopore immersed in 250 mM *NaCl* electrolyte (blue circles) is shown along with FES simulations of it.

SUPPLEMENTAL FIGURE 2.

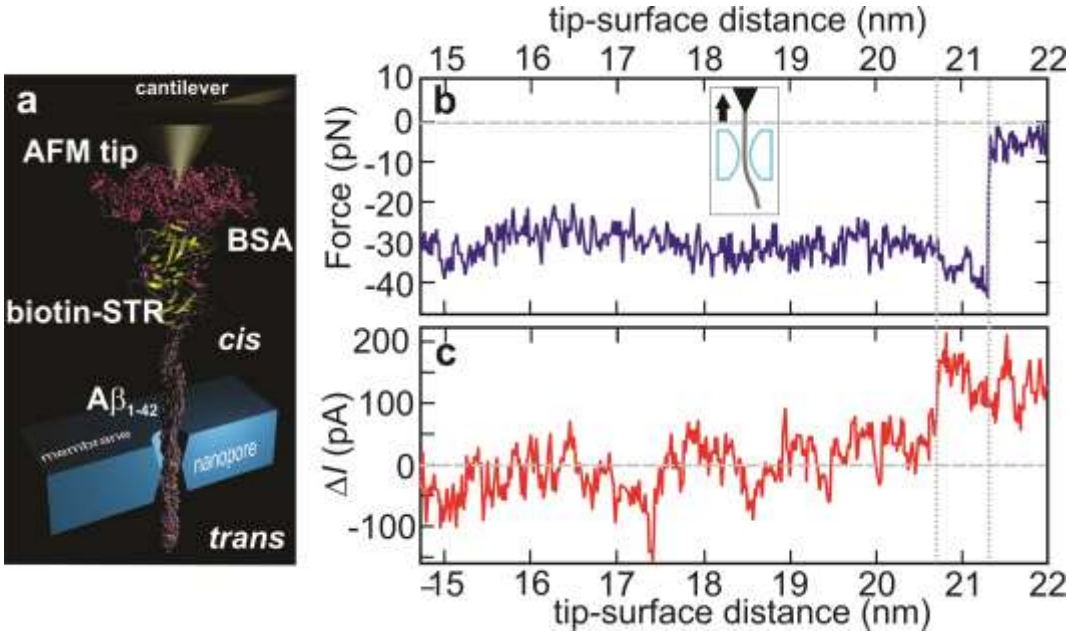

SUPPLEMENTAL FIGURE 2. The forces and blockade current measured as a single Aβ$_{1-42}$ peptide was impelled relatively frictionless through a *sub*-nanopore. (a) A schematic cutaway of the experiment showing a biotinylated Aβ$_{1-42}$ peptide tethered to the tip of an AFM cantilever through a bond to streptavidin (STR), translocating through the *sub*-nanopore. A denatured, tethered peptide-SDS aggregate was advanced by the AFM toward the *sub*-nanopore,

captured and threaded through it by the electric field, and then retracted from it at a constant velocity, while the tip deflection and current were recorded to measure the force and blockade current. **(b,c)** Concomitant measurements of the force and current are shown as the $A\beta_{1\text{-}42}$ peptide was impelled through a *sub*-nanopore with a 0.8×0.9 nm^2 cross-section at the waist spanning an *a-Si* membrane nominally 5 nm thick. Both the *cis*- and *trans*-sides of the membrane were immersed in 0.01% (w/v) SDS in a 250 mM *NaCl* solution. (The *sub*-nanopore cross-section was measured *in situ* immediately after sputtering, but the actual cross-section was likely reduced after exposure to the ambient.) Changes in both the force (b) and the pore current (c) were observed while the AFM cantilever was retracted from the pore at velocity of 2.0 nm/s. The change in the force (b) on the protein that is observed near 21.3 nm is an indication that the electric force on the molecule associated with an applied potential of +0.70 V was terminated. The change in the pore current (c) observed near 20.7 nm indicates the position where the blockade in the pore current was relieved. Only a small force (24 ± 5 pN) was required to extract the molecule from the *sub*-nanopore and relieve the ΔI = 130 ±40 pA current blockade. The force hardly varied over the distance of the extraction and so it is referred to as "frictionless". **(b, inset)** The cartoon shows the assumed molecular configuration with the arrow indicating the direction of the cantilever motion.

SUPPLEMENTAL FIGURE 3.

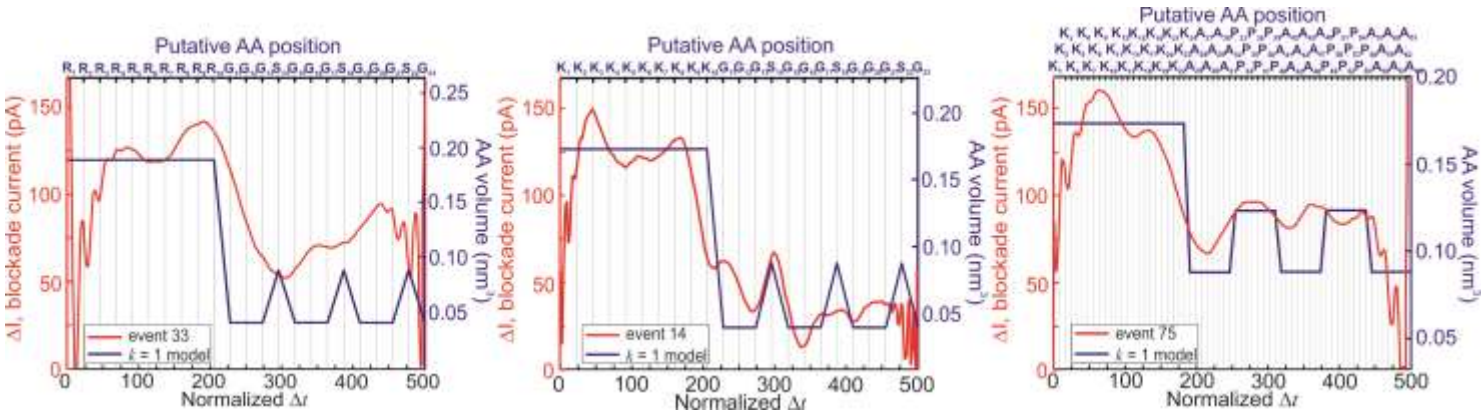

SUPPLEMENTAL FIGURE 3. Testing the sensitivity of a *sub*-nanopore to molecular volume using block co-polymers. (a-c) Single blockade currents, ΔI, acquired three block co-polymers *block-p*$(R)_{10}$-*co*-$(G_3S)_3$-G 23 AAs long (denoted by R-G-S), *block-p*$(K)_{10}$-*co*-$(G_3S)_3$-G 23 AAs long (denoted by K-G-S) and *block-p*$(K)_{24}$-*co*-$(A_8P_8)_2$-A_8 48 AAs long (denoted by K-A-P), respectively, using the same *sub*-nanopore, which was 0.6 nm in diameter at the waist (ER153). These block co-polymers were used as controls to gauge the read accuracy (from the amplitude) and resolution (from the slope between the blocks) of the *sub*-nanopore using a 250 kS/s sampling rate and a < 100 kHz bandwidth. The empirical data is plotted versus normalized blockade duration for comparison. Juxtaposed with the empirical data is a naïve volume model (assuming k = 1, red line) plotted versus putative acid position assuming a uniform AA velocity through the pore. The data was acquired with a bias voltage of 0.30–0.40 V applied across the membrane in electrolyte containing 100 pM of the peptide, 250 mM *NaCl* and 265.5 nM SDS and 1 mM β-ME. The abrupt steps in data shown are commensurate with large volume changes between Arg(R, 0.1734 nm^3) and Gly(G, 0.0601 nm^3) $\Delta V = 0.1133\, nm^3$, Lys(K, 0.1686 nm^3) and Gly $\Delta V = 0.1085\, nm^3$, and Lys(K, 0.1686 nm^3) and Ala(A, 0.0878 nm^3) $\Delta V = 0.0808\, nm^3$. Likewise, the sharp slope between R and G, and K and G were also consistent with single

residue resolution (k = 1). Beyond the steps, the subtle modulations of fluctuation amplitudes between Ser(S, 0.089 nm^3) and Gly indicate that differences as small as ($\Delta V = 0.00289\, nm^3$) could be detected this way.

SUPPLEMENTAL FIGURE 4.

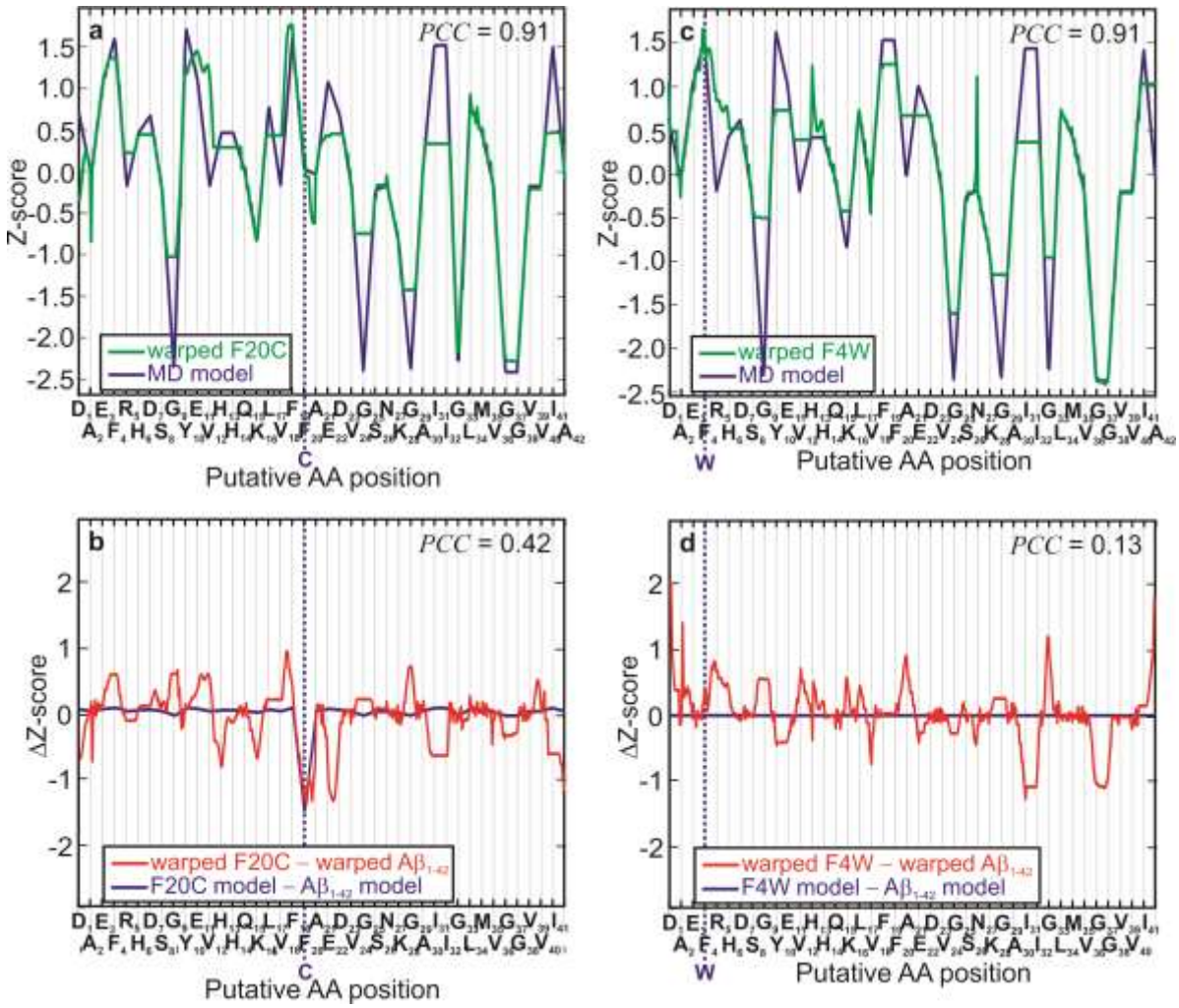

SUPPLEMENTAL FIGURE 4. Proteoform sequence analysis with near single acid resolution using a *sub*-nanopore. (a,c) Empirical consensuses associated with blockades due to two mutants of $A\beta_{1\text{-}42}$, F20C and F4W, respectively, are shown after alignment to the corresponding MD models versus the putative AA positions (green lines). Juxtaposed with the empirical consensuses are the corresponding MD models for each variant (blue lines). The dotted

blue lines indicate the site of the mutation. The aligned consensuses were all well correlated to the respective volume models with *PCC* ≥ 0.91. **(b,d)** The differences in the Z-scores between the aligned consensus for $A\beta_{1\text{-}42}$ and the respective aligned consensuses for the variants in (a,c) (red lines) are shown versus the putative AA positions. (The $A\beta_{1-42}$ reference data used for comparison—see Fig. 3e—was nearly perfectly aligned with the respective MD model *PCC* = 0.95.) Juxtaposed on the same plots are the differences in the Z-scores between the respective MD models for $A\beta_{1\text{-}42}$ and the corresponding variants (blue lines). The difference between the empirical consensuses were correlated to the difference in the corresponding models (0.13 < *PCC* < 0.42).

SUPPLEMENTAL VIDEOAB1-42E. A molecular dynamics simulation visualizing the translocation of beta-amyloid through a sub-nanopore.

Following the scheme outlined in the METHODS, visual molecular dynamics (VMD) snapshots are compiled into a video depicting $A\beta_{1\text{-}42}$ translocating across a 5 nm thick silica membrane through a *sub*-nanopore with a bi-conical topography with a cone angle of 8° near the waist, expanding to 36° near each orifice that mimicks the STEM image shown in Fig. 1d. To construct the *sub*-nanopore, initially a crystalline silica slab was generated with a number of unit cells required to fill the pore excluded volume of the amorphous silica (SiO_2) membrane with a density of 3.0 g/cm^3. The surface geometry of a double conical *sub*-nanopore having an elliptical cross-section was modeled using the relation:

$$\sqrt{\tan^2(\alpha)\cdot x^2+\tan^2(\beta)\cdot y^2} < \sqrt{a\cos^2(\Phi)+b\sin^2(\Phi)\cdot\tan(\alpha)\cdot\tan(\beta)}+|z|\tan(\alpha)\cdot\tan(\beta)+\delta$$

where α, β are the cone angles at semi-major (a) and -minor (b) axis of the ellipse (at the minimum cross-section of the *sub*-nanopore near the waist), Φ is the angle between x-axis and a position vector of atoms inside the *sub*-nanopore in x-y plane and δ is the van der Waals radii of

the pore surface atoms (taken as 0.16 nm). The *Si* and *O* atoms were randomly placed inside the membrane, excluding the volume of *sub*-nanopore, and then the entire membrane was subjected to simulated annealing a high temperature 7000 K. A repulsive grid potential was applied to avoid the entry of SiO_2 atoms inside the *sub*-nanopore and CHARMM force field parameters were used for *Si* and *O* atoms in the membrane. Later, the bonds between the *Si* and *O* atoms of silica were defined using a 0.22 nm distance cut-off. Using this protocol, a silica *sub*-nanopore having 0.5×0.8 nm^2 minimum cross section was created with a realistic topography (Fig. 1d).

The coordinates of $A\beta_{1\text{-}42}$ (pdbcode:1IYT) protein structure were downloaded from the protein data bank (PDB). The protein structure was placed at the orifice of the pore to study their translocations through the silica *sub*-nanopore and CHARMM36 force field parameters were employed. The constructed silica *sub*-nanopore-protein complex was solvated with a 5 nm thick TIP3P water film on either side of the pore to screen the electrostatic interactions of the pore with its periodic images. The Na^+ and Cl^- counter ions were added to the solvated *sub*-nanopore to set 200 mM *NaCl* concentration. Initial systems were subjected to 2000 steps of conjugate-gradient minimization to remove the bad contacts and followed by 1 ns NPT equilibration at temperature 300 K with a 1 fs time step for integration to achieve the bulk water density to 1.0 g/cm^3. Periodic boundary conditions were used in all three directions.

A Nośe–Hoover thermostat with a damping coefficient of 1 ps was connected to silica atoms of the membrane to maintain the temperature. Subsequently, the equilibrated systems were subjected to a 20 ns NVT MD simulation with a 0.12 nm cutoff for calculating the short-range part of the non-bonding interactions and the long-range electrostatic interactions were calculated using Particle-Mesh-Ewald (PME) method. The equilibrated *sub*-nanopore system was subjected to an external applied electric field for 25 ns to obtained steady-state ionic current and the last 5 ns trajectory was used to obtained current-voltage characteristics of the *sub*-nanopore.

To simulate the translocation of a peptide, the molecular force fields describing water, ions, and the peptide were combined with the CHARMM force fields for the SiO_2 in a 5 nm thick membrane. To mimic the experiments, the membrane separated an aqueous solution of *NaCl* into two compartments connected by a bi-conical *sub*-nanopore with a 0.5×0.8 nm^2 cross-section at the waist to match the topography and (linear) current-voltage characteristics (0.194 nS in MD compared to 0.3 nS empirically) of the pore.

At first, electrophoresis was used to force the peptide into the pore alone, but the competition with ions near the membrane and/or non-specific binding of the acids to the surface pinned the molecule in a spot for an extended duration, blocking the ion flow. Alternatively, the peptide was impelled through the *sub*-nanopore by applying a voltage of 25 V across the membrane with a zero-acceleration velocity of 8×10^{-5} nm/ps.